

# Predicting parametric spatiotemporal dynamics by multi-resolution PDE structure-preserved deep learning

Xin-Yang Liu<sup>1</sup>, Hao Sun<sup>2,3</sup>, Min Zhu<sup>4</sup>, Lu Lu<sup>4</sup>, and Jian-Xun Wang<sup>1,5,6\*</sup>

<sup>1</sup>Department of Aerospace and Mechanical Engineering, University of Notre Dame, Notre Dame, IN, USA

<sup>2</sup>Gaoling School of Artificial Intelligence, Renmin University of China, Beijing, China

<sup>3</sup>Beijing Key Laboratory of Big Data Management and Analysis Methods, Beijing, China

<sup>4</sup>Department of Chemical and Biomolecular Engineering, University of Pennsylvania, Philadelphia, PA, USA

<sup>5</sup>Lucy Family Institute for Data & Society, University of Notre Dame, Notre Dame, IN, USA

<sup>6</sup> Center for Sustainable Energy (ND Energy), University of Notre Dame, Notre Dame, IN, USA

\*Corresponding author. E-mail: jwang33@nd.edu

## Abstract

Pure data-driven deep learning models suffer from high training costs, error accumulation, and poor generalizability when predicting complex physical processes. A more promising way is to leverage our prior physics knowledge in scientific deep learning models, known as physics-informed deep learning (PiDL). In most PiDL frameworks, the physics prior is utilized to regularize neural network training by incorporating governing equations into the loss function. The resulting physical constraint, imposed in a soft manner, relies heavily on a proper setting of hyperparameters that weigh each loss term. To this end, we propose a new direction to leverage physics prior knowledge by “baking” the mathematical structure of governing equations into the neural network architecture, namely PDE-preserved neural network (PPNN). The discretized PDE is preserved in PPNN as convolutional residual networks formulated in a multi-resolution setting. This physics-inspired learning architecture endows PPNN with excellent generalizability and long-term prediction accuracy compared to the state-of-the-art black-box baselines. The effectiveness and merit of the proposed methods have been demonstrated over a handful of spatiotemporal dynamical systems governed by spatiotemporal PDEs, including reaction-diffusion, Burgers’, and Navier-Stokes equations.

**Keywords:** Physics-informed deep learning, Scientific machine learning, Surrogate modeling, Operator learning, Residual connection, Computational fluid dynamics

## INTRODUCTION

Computational modeling and simulation capabilities play an essential role in understanding, predicting, and controlling various physical processes (e.g., turbulence, heat-flow coupling, and fluid-structure interaction), which often exhibit complex spatiotemporal dynamics. These physical phenomena are usually governed by partial differential equations (PDEs) and can be simulated by solving these PDEs numerically based on, e.g., finite difference (FD), finite volume (FV), finite element (FE), or spectral methods. However, predictive modeling of complex spatiotemporal dynamics using traditional numerical methods can be significantly challenging in many practical scenarios: (1) governing equations for complex systems might not be fully known due to a lack

of complete understanding of the underlying physics, for which a first-principled numerical solver cannot be built; (2) conventional numerical simulations are usually time-consuming, making it infeasible for many applications that require many repeated model queries, e.g., optimization design, inverse problems, and uncertainty quantification (UQ), attracting increasing attention in scientific discovery and engineering practice.

Recent advances in scientific machine learning (SciML) and ever-growing data availability open up new possibilities to tackle these challenges. In the past few years, various deep neural networks (DNNs) have been designed to learn the spatiotemporal dynamics in latent spaces enabled by proper orthogonal decomposition (POD) [1–4] or convolutional encoding-decoding operations [5–8]. In particular, fast neural simulators based on graph neural networks (GNN) have been proposed and demonstrated to predict spatiotemporal physics on irregular domains with unstructured meshes [9, 10]. Although showing good promise, most of these works are purely data-driven and black-box in nature, which rely on “big data” and may have poor generalizability, particularly in out-of-sample regimes in the parameter space. As a more promising strategy, baking physics prior knowledge (e.g., conservation laws, governing equations, and constraints) into deep learning is believed to be very effective to improve its sample efficiency and generalizability [11], here referred to as physics-informed deep learning (PiDL). An impressive contribution in this direction is physics-informed neural networks (PINNs) [12], where well-posed PDE information is leveraged to enable deep learning in data-sparse regimes. The general idea of PINNs is to learn (or solve) the PDE solutions with DNNs, where the loss functions are formulated as a combination of the data mismatch and residuals of known PDEs, unifying forward and inverse problems within the same DNN optimization framework. The merits of PINNs have been demonstrated over various scientific applications, including fast surrogate/meta modeling [13–15], parameter/field inversion [16–19], and solving high-dimensional PDEs [20, 21], to name a few. Due to the scalability challenges of the point-wise fully-connected PINN formulation to learn continuous functions [22–24] or operators [25–28], many remedies and improvements in terms of training and convergence have been proposed [29–31]. In particular, there is a growing trend in developing field-to-field discrete PINNs by leveraging convolution operations and numerical discretizations, which have been demonstrated to be more efficient in spatiotemporal learning [32, 33]. For example, convolution neural networks (CNN) or graph convolution networks (GCN) were built to approximate the discrete PDE solutions, where the PDE residuals can be formulated in either strong or weak forms by finite-difference [34–36], finite volume [37], or finite element methods [38–42]. Moreover, recurrent network formulation informed by discretized PDEs have been developed for spatiotemporal dynamic control using model-based reinforcement learning [43].

In the PINN framework, the term “physics-informed” mainly refers to imposing PDE residuals in the loss or likelihood functions to regularize/drive DNN training. However, it remains unclear how to leverage physics-induced bias, i.e., (partially) known governing equations, to inform the *learning architecture design*, which is the focus of this work. Recent studies have revealed the connection between neural network structures and ordinal/partial differential equations (ODEs/PDEs) [44–49]. For example, Lu et al. [45] bridged deep convolutional network architectures and numerical differential equations. Chen et al. [50] showed that the residual networks (ResNets) [51] can be interpreted as the explicit Euler discretization of an ODE, while ODEs can be used to formulate the continuous residual connection with infinite depths, known as the NeuralODE [52]. Motivated by differential equations, novel deep learning architectures have been recently developed in the computer science community, e.g., new convolutional ResNets guided by parabolic and hyperbolic PDEs [47], GRAND as a graph network motivated by diffusion equations [48], and PDE-GCN motivated by hyperbolic PDEs to improve over-smooth issues in deep graph learning [49]. However, these studies mainly aimed to develop generic DNN architectures with some desired features by utilizing specific

properties of certain PDEs (e.g., diffusion, dispersion, etc.), and the designed neural networks are not necessarily used to learn the physical processes governed by those PDEs. In this paper, we are interested in the design of novel learning architectures for predicting spatiotemporal dynamics by preserving their governing PDEs in the discrete forms as convolution operations. This study explores PIDL in novel learning architecture design, along the line of differentiable programming ( $\partial P$ ), which is a generic concept of extending DNNs to more general computer programs that can be trained in the same way as deep learning models do [53]. In general, a  $\partial P$  model is formulated by marrying DNNs with a fully differentiable physics-based solver, and thus the gradients can be back-propagated through the entire hybrid neural solver based on automatic differentiation (AD) or discrete adjoint methods. Relevant works include universal differential equations (UDE) [54], NeuralPDE [55], and others, where DNNs are formulated within a differentiable PDE solver for physics-based modeling. In particular, this idea has been recently explored in predictive modeling of rigid body dynamics [56, 57], epidemic dynamics [58], and fluid dynamics [59–61]. These studies imply great promise of incorporating physics-induced prior (i.e., PDE) into DNN architectures.

In this work, we propose a novel PDE structure-preserved deep learning framework for rapidly predicting parametric spatiotemporal dynamics, where the network architecture design is inspired by the governing PDEs, discretized in a multi-resolution setting. Specifically, we develop a new auto-regressive neural solver based on convolutional ResNet framework, where the residual connections are constructed by preserving the governing PDE structures, which are (partially) known *a priori*, discretized on low-resolution grids, while encoding-decoding convolution operations with trainable filters enable high-resolution state predictions on fine grids. Compared to classic ResNets with black-box residual connections, the proposed PDE-preserved neural network (PPNN) is expected to be superior in terms of both training efficiency and out-of-sample generalizability for, e.g., unseen boundary conditions and parameters, and extrapolating in time. The contributions of this work are summarized as follows: (i) an innovative physics-inspired learning architecture design is presented, where the PDE structures are preserved by the residual connection; (ii) multi-resolution information passing through network layers is proposed to stabilize long-term model rollout predictions over large time steps; (iii) the superiority of the proposed PPNN is demonstrated for PDE operator learning in terms of training complexity, extrapolability, and generalizability in comparison with the baseline black-box ResNet model, using a series of comprehensive numerical experiments on spatiotemporal dynamics governed by various parametric unsteady PDEs, including reaction-diffusion equations, Burgers’ equations, and unsteady Navier-Stokes equations.

## RESULTS

### Learning spatiotemporal dynamics governed by PDEs

We consider a multi-dimensional spatiotemporal system of  $\mathbf{u}(\mathbf{x}, t; \boldsymbol{\lambda})$  governed by a set of non-linear coupled PDEs parameterized by  $\boldsymbol{\lambda} \in \mathbb{R}^d$ , which is a  $d$ -dimensional parameter vector, while  $\mathbf{x}$  and  $t$  are spatial and temporal coordinates, respectively. Our goal is to develop a data-driven neural solver for rapid predictions of spatiotemporal dynamics given different parameters  $\boldsymbol{\lambda}$ . The neural solver is formulated as a next-step DNN model by learning the dynamic transitions from the current step  $t$  to the next time step  $t + \Delta t$  ( $\Delta t$  is the time step).

This study focuses on the learning architecture design for improving the robustness, stability, and generalizability of data-driven next-step predicting models, which commonly suffer from considerable error accumulations due to the auto-regressive formulation and fails to operate in a long-span model rollout. In contrast to existing models which are black-box, we propose a novel PDE-preserved neural network (PPNN) architecture inspired by the relationship between network structures and

PDEs, by hypothesizing that the predictive performance can be significantly improved if the network is constructed by preserving (partially) known governing PDEs of the spatiotemporal dynamics to be learned. Specifically, the known portion of the governing PDEs in discrete forms are preserved in residual connection blocks. As shown in Fig. 1a, the PPNN architecture features a residual connection which consists of two parts: a trainable network and a PDE preserving network, where the right hand side (RHS) of the governing PDE, discretized on finite difference grid, is represented by a convolution neural network. The weights of the PDE preserved convolutional residual component are determined by the discretization scheme and remain constant during training.

However, in practice, neural solvers are expected to roll out much faster than numerical solvers, and the time step  $\Delta t$  would be orders of magnitude larger than that used in conventional numerical solvers, which may lead to catastrophic stability issues if naively embedding the discretized PDE into the neural network. To this end, we implement a multi-resolution PPNN based on the convolutional (conv) ResNet backbone (shown in Fig. 1b), where PDE-preserving blocks work on a coarse grid to enable stable model rollout with large evolving steps. This is achieved by using the bilinear down-sampling and bicubic up-sampling algorithms to auto-encode the PDE-preserved hidden feature in a low-resolution space, which is then fed into the main residual connection in the original high-resolution space. Together with the trainable block, which consists of decoding-encoding convResNet blocks defined on the fine mesh, PPNN enables predictions at a high resolution. Moreover, the network is conditioned on physical parameters  $\lambda$ , enabling fast parametric inference and generalizing over the high-dimensional parameter space. (More details are discussed in the [METHODS](#) section.)

In this section, we evaluate the proposed PDE structure-preserved neural network (PPNN) on three nonlinear systems with spatiotemporal dynamics, where the governing PDEs are known or partially-known *a priori*. Specifically, the spatiotemporal dynamics governed by FitzHugh-Nagumo reaction diffusion (RD) equations, Burgers’ equations, and incompressible Navier-Stokes (NS) equations with varying parameters  $\lambda$  (e.g., IC, diffusion coefficients, Reynolds number, etc.) in 2D domains are studied. In particular, we will study the scenarios where either fully-known or incomplete/inaccurate governing PDEs are preserved. To demonstrate the merit of preserving the discrete PDE structure in ConvResNet, the proposed PPNN is compared with a state-of-the-art (SOTA) black-box ConvResNet next-step model as a baseline, which is a CNN variant of the Mesh-GraphNet [9] (see section [Next-step prediction models based on convolutional ResNets](#)). For a fair comparison, the network architecture of the trainable portion of the PPNN is the same as the black-box baseline model. Moreover, all models are compared on the same sets of training data in each test case. The generalizability, robustness, training and testing efficiency of the PPNN are investigated in comparison with the SOTA baseline. Moreover, the relationship between the PDE-preserving portion of PPNN and numerical solvers is discussed. Note that we use the same network setting, i.e., same network structure, hyperparameters and training epochs, for all the test cases (except for the NS system, which has slight modifications adapting to three state variables). More details about the neural network settings can be found in Section 1 in supplementary materials.

All the DNN predictions are evaluated against the high-resolution fully-converged numerical solutions as the reference using a full-field error metric  $\epsilon_t$  defined at time step  $t$  as,

$$\epsilon_t = \frac{1}{N} \sum_{i=1}^N \frac{\|f_\theta(\hat{\mathbf{u}}_{t-1}, \lambda_i | \tilde{\theta}) + \hat{\mathbf{u}}_{t-1} - \mathbf{u}_t(\lambda_i)\|_2}{\|\mathbf{u}_t(\lambda_i)\|_2}, \quad (1)$$

where  $N$  indicates the number of the testing physical parameters  $\lambda_i$ ,  $\mathbf{u}_t(\lambda_i)$  is the reference solution at time step  $t$  corresponding to the physical parameter  $\lambda_i$ ,  $f_\theta$  represents the trained neural network function with optimized weights  $\tilde{\theta}$ , and  $\hat{\mathbf{u}}_{t-1}$  represents the state predicted by the model at previous

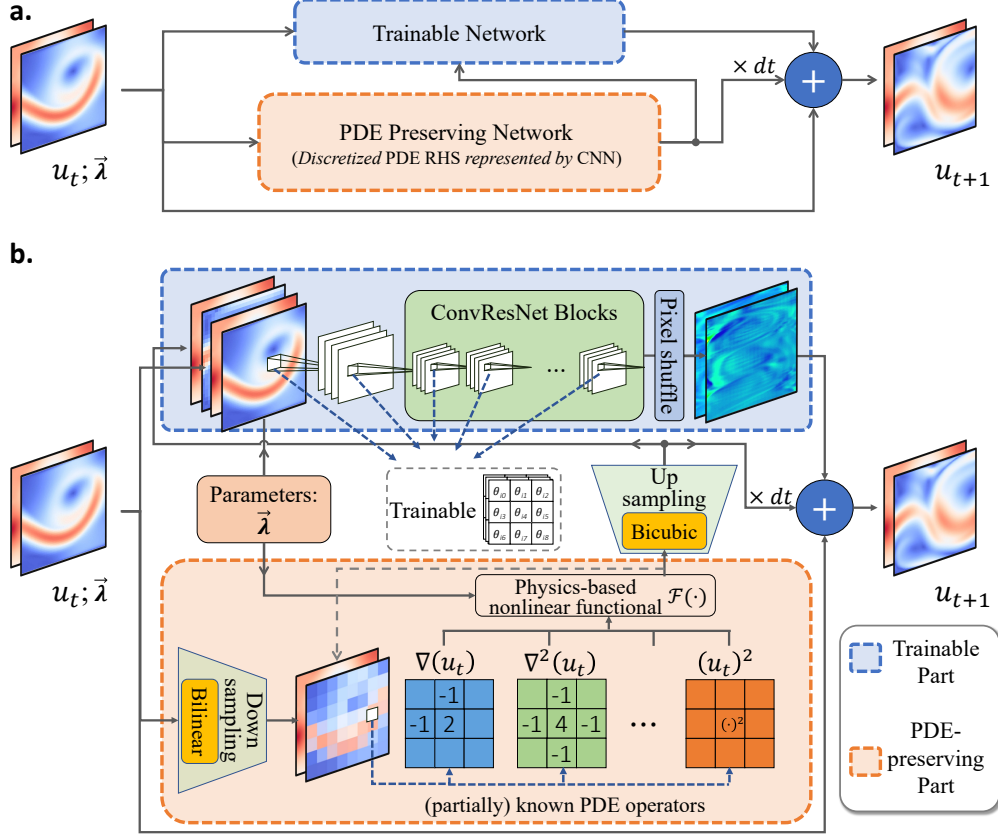


**Figure 1:** **a.** Schematic diagram of the proposed PDE-preserved neural network (PPNN). **b.** A detailed implementation schematic of the ConvResNet-based, multi-resolution PPNN studied in this paper.

time step  $t - 1$ ,

$$\begin{aligned}\hat{\mathbf{u}}_t &= f_\theta(\hat{\mathbf{u}}_{t-1}, \boldsymbol{\lambda}_i | \boldsymbol{\theta}) + \hat{\mathbf{u}}_{t-1}, \quad t \in [2, n] \\ \hat{\mathbf{u}}_1 &= f_\theta(\mathbf{u}_0(\boldsymbol{\lambda}_i), \boldsymbol{\lambda}_i | \boldsymbol{\theta}) + \mathbf{u}_0(\boldsymbol{\lambda}_i)\end{aligned}\quad (2)$$

where  $n$  is the number of testing steps,  $\mathbf{u}_0(\boldsymbol{\lambda}_i)$  represents the initial condition given  $\boldsymbol{\lambda}_i$ . For brevity, numerical details for each case are given in Section 2 of the supplementary materials.

## When the governing PDEs are fully known

We herein consider three well-known spatiotemporal PDEs (e.g., the FitzHugh–Nagumo reaction diffusion equations, the Viscous Burgers’ equation and the Navier-Stokes equations) when the closed-form equations are fully known.

**FitzHugh–Nagumo reaction diffusion equations** We first consider a spatiotemporal dynamic system governed by the FitzHugh–Nagumo equations with periodic BCs, which is a generic model for excitable media. The main part of the FitzHugh–Nagumo model is reaction-diffusion (RD) equations,

$$\frac{\partial \mathbf{u}}{\partial t} = \gamma \nabla^2 \mathbf{u} + \mathbf{R}(\mathbf{u}), \quad t \in [0, T], \quad (3)$$

where  $\mathbf{u} = [u(x, y, t), v(x, y, t)]^T \in \mathbb{R}^2$  are two interactive components,  $\gamma$  is the diffusion coefficient,  $T = 0.2\text{s}$  is the time length we simulated, and  $\mathbf{R}(\mathbf{u}) = [R_u(u, v), R_v(u, v)]^T$  are source terms for

the reaction,

$$\begin{aligned} R_u(u, v) &= u - u^3 - v + \alpha, \\ R_v(u, v) &= \beta(u - v), \end{aligned} \quad (4)$$

where  $\alpha = 0.01$  represents the external stimulus and  $\beta = 0.25$  is the reaction coefficient. The initial condition (IC)  $\mathbf{u}_0$  is a random field and generated by randomly sampling from a normal distribution,

$$u(x, y, 0), v(x, y, 0) \sim \mathcal{N}(0, 1), \quad (5)$$

which is then linearly scaled to  $[0.1, 1.1]$ . Given different ICs and diffusion coefficients  $\gamma$ , varying dynamic spatial patterns of neuron activities can be simulated. Here, the next-step neural solvers are trained to learn and used to predict the spatiotemporal dynamics of varying modeling parameters (i.e., ICs and diffusion coefficients). Namely, we attempt to build a surrogate model in a very high-dimensional parameter space  $\boldsymbol{\lambda} \in \mathbb{R}^d$ , where  $d = 65,537$ , since the dimensions for IC and diffusion coefficient are  $256^2$  and 1, respectively. The reference solutions are obtained on the simulation domain  $(x, y) \in [0, 6.4] \times [0, 6.4]$ , discretized with a fine mesh of  $256 \times 256$  grids, based on the finite difference method.

Figure 2a shows the PPNN-predicted solution snapshots of the RD equations at four randomly selected test parameters (i.e., randomly generated ICs and unseen diffusion coefficients). The prediction results of baseline black-box ConvResNet (first row) and the proposed PPNN (second row) are compared against the ground truth reference (third row). It can be seen that both models agree with the reference solutions for  $t < 0.6T$ , showing good generalizability on testing ICs and  $\gamma$  for a short-term model rollout. However, the error accumulation becomes notable for the black-box baseline when  $t > T$ , and the spatial patterns of the baseline predictions significantly differ from the reference at  $t = 2T$ , which is an expected issue for the next-step predictors. In contrast, the results of our PPNN have an excellent agreement with the reference solutions over the entire time span  $[0, 2T]$  on all testing parameters, showing great robustness, predictability, and generalizability in both the spatiotemporal domain and parameter space. Predicted solutions on more testing parameters are presented in Fig. 3.

To further examine the error propagation in time for both models, the relative testing errors  $\epsilon_t$  averaged over 100 randomly selected parameters in training and testing sets are computed and plotted in Fig. 2, where Fig. 2b shows the averaged model-rollout error evaluated on 100 training parameters and the Fig. 2c shows the error averaged on 100 randomly generated testing parameters. The model is only trained within the range of  $1T$  ( $100\Delta t$ ), and it is clearly seen that the rollout error of the black-box model notably grows in the extrapolation range  $[T, 2T]$  (from  $100\Delta t$  to  $200\Delta t$ ), where  $\Delta t = 200\delta t$  is the learning stepsize which is 200 numerical timesteps  $\delta t$ . The error accumulation becomes more severe for the unseen testing parameters. However, our PPNN predictions maintain an impressively low error, even when extrapolating twice the length of the training range. Besides, the scattering of the error ensemble is significantly reduced compared to the black-box baseline, indicating great robustness of the PPNN for various testing parameters.

**Viscous Burgers' equation** For the second case, we study the spatiotemporal dynamics governed by the viscous Burgers' equations on a 2D domain with periodic boundary conditions,

$$\frac{\partial \mathbf{u}}{\partial t} + \mathbf{u} \cdot \nabla \mathbf{u} = \nu \nabla^2 \mathbf{u}, \quad t \in [0, T], \quad (6)$$

where  $\mathbf{u} = [(u(x, y, t), v(x, y, t))]^T \in \mathbb{R}^2$  is the velocity vector,  $T = 2\text{s}$  is the time length we simulated, and  $\nu$  represents the viscosity. The initial condition (IC)  $\mathbf{u}_0$  is generated according to,

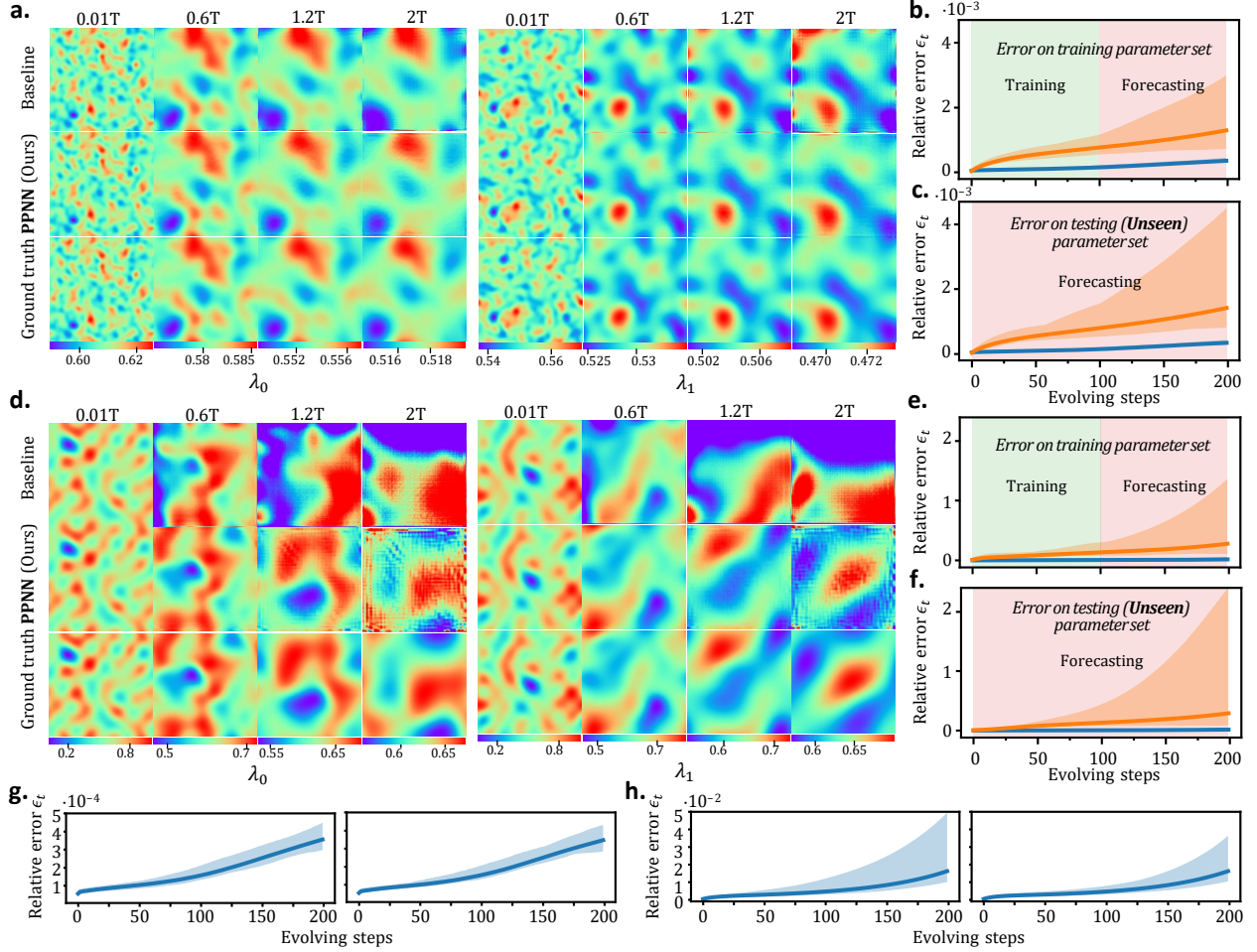


**Figure 2:** **a** and **d**, Predicted solution snapshots of  $u$  for the RD equations (**a**), and the velocity magnitude  $\|u\|_2$  for the Burgers' equations (**d**) at different time steps and unseen parameters, obtained by black-box ConvResNet (baseline model, first rows), and PPNN (our method, second rows), compared against ground truth (high-resolution FD simulation, third rows).  $\lambda_0, \lambda_1$  are randomly selected testing (unseen) parameters in each system. **b-c**, Relative prediction error  $\epsilon_t$  of PPNN (—) and black-box ConvResNet baseline (—) for the RD dynamics (**b-c**) and Burgers' equations (**e-f**), averaged on 100 randomly sampled training parameters  $\lambda$  (**b, e**) and testing (*unseen*) parameters (**c, f**). The shaded area shows the maximum and minimum relative errors of all testing trajectories. **g** Zoom in views of the relative error curve of PPNN shown in **b** (left) and **c** (right). **h** Zoom in views of the relative error curve of PPNN shown in **b** (left) and **c** (right).

$$\mathbf{u}_0 = \begin{cases} u_0 = \sum_{i=-4}^4 \sum_{j=-4}^4 r_{i,j}^{(1)} \sin(ix + jy) + r_{i,j}^{(2)} \cos(ix + jy) \\ v_0 = \sum_{i=-4}^4 \sum_{j=-4}^4 r_{i,j}^{(3)} \sin(ix + jy) + r_{i,j}^{(4)} \cos(ix + jy) \end{cases} \quad r_{i,j}^{(k)} \sim \mathcal{N}(0, 1); k = 1, 2, 3, 4, \quad (7)$$

where  $x, y$  are spatial coordinates of grid points, and  $r_{i,j}^{(k)}; k \in 1, 2, 3, 4$  are random variables sampled independently from a normal distribution. The IC is normalized in the same way as mentioned in the RD case. We attempt to learn the dynamics given different ICs and viscosities. Similar to the RD cases, the parameter space  $\mathbb{R}^d$  is also high-dimensional ( $d = 324$ ), as the IC is parameterized by  $4 \times 9^2$  independent random variables and the scalar viscosity can also vary in range  $[0.02, 0.07]$ . The reference solution is generated by solving the Burgers' equations on the domain of  $(x, y) \in [0, 3.2]^2$ ,

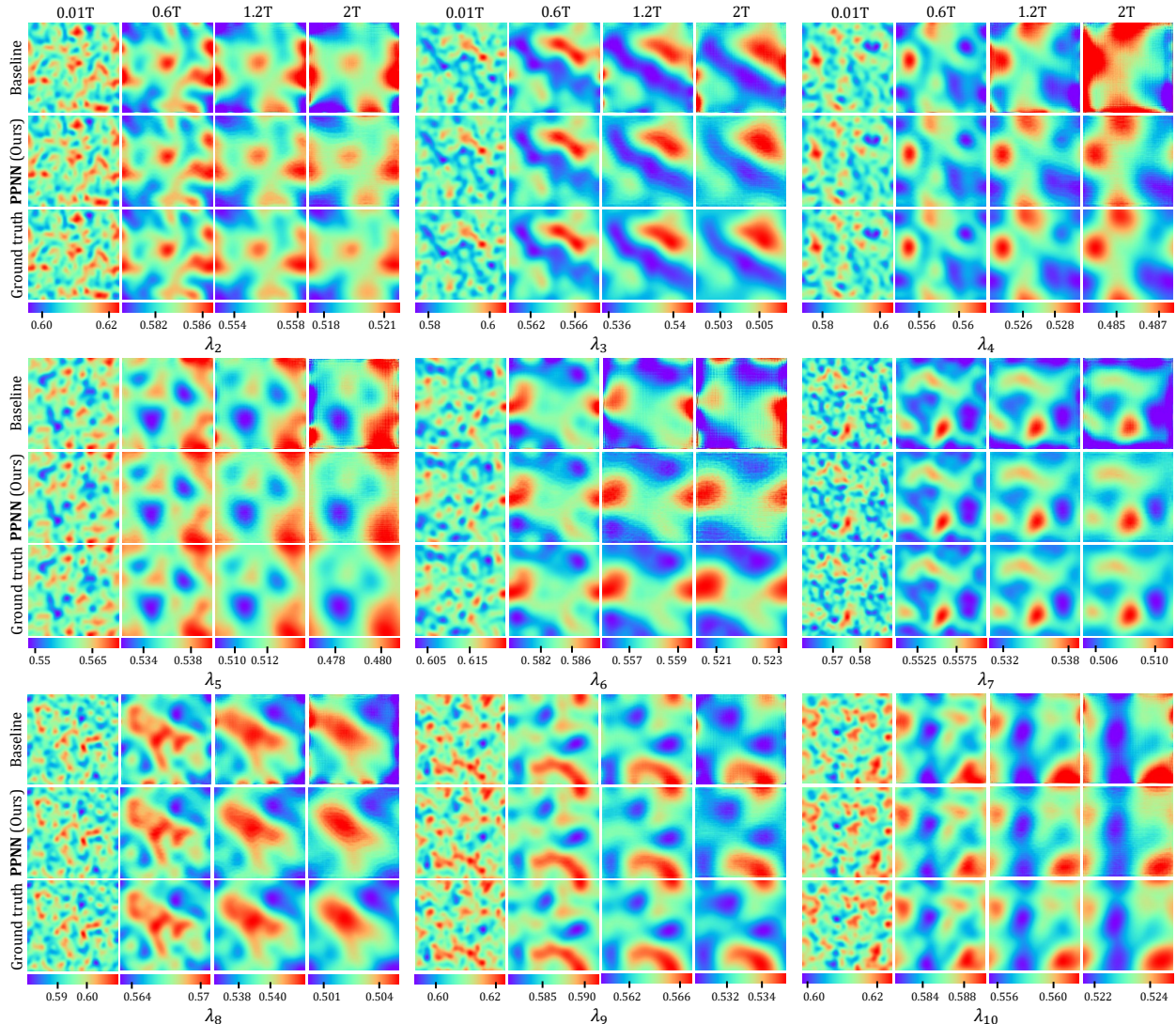


**Figure 3:** Predicted solution snapshots of reactant  $u$  for the RD equations, obtained by black-box ConvResNet (baseline), and PPNN (ours); compared against ground truth. where  $\lambda_2 - \lambda_{10}$  are testing parameters, which are not in the training set.

discretized by a fine mesh of  $256 \times 256$  grids using finite difference method. The velocity magnitude contours of the 2D Burgers' equation with different testing parameters are shown in Fig. 2d, obtained by the black-box baseline, PPNN, and reference numerical solver, respectively. Note that all the testing parameters are not seen during training. (More predicted solutions on different testing parameters are presented in Fig. 4.) Similar to the RD case, PPNN shows a significant improvement over the black-box baseline in terms of long-term rollout error accumulation and generalizability on unseen ICs and viscosity  $\nu$ . Due to the strong convection effect, black-box baseline predictions deviate from the reference very quickly, and significant discrepancies in spatial patterns can be observed as early as  $t < 0.6T$ . In general, the black-box baseline notably suffers from the poor out-of-sample generalizability for unseen parameters, making the predictions useless. Our PPNN significantly outperforms the black-box baseline, and its prediction results agree with the reference for all testing samples. Although slight prediction noises are present after a long-term model rollout ( $t > 1.2T$ ), the overall spatial patterns can be accurately captured by the PPNN even at the last

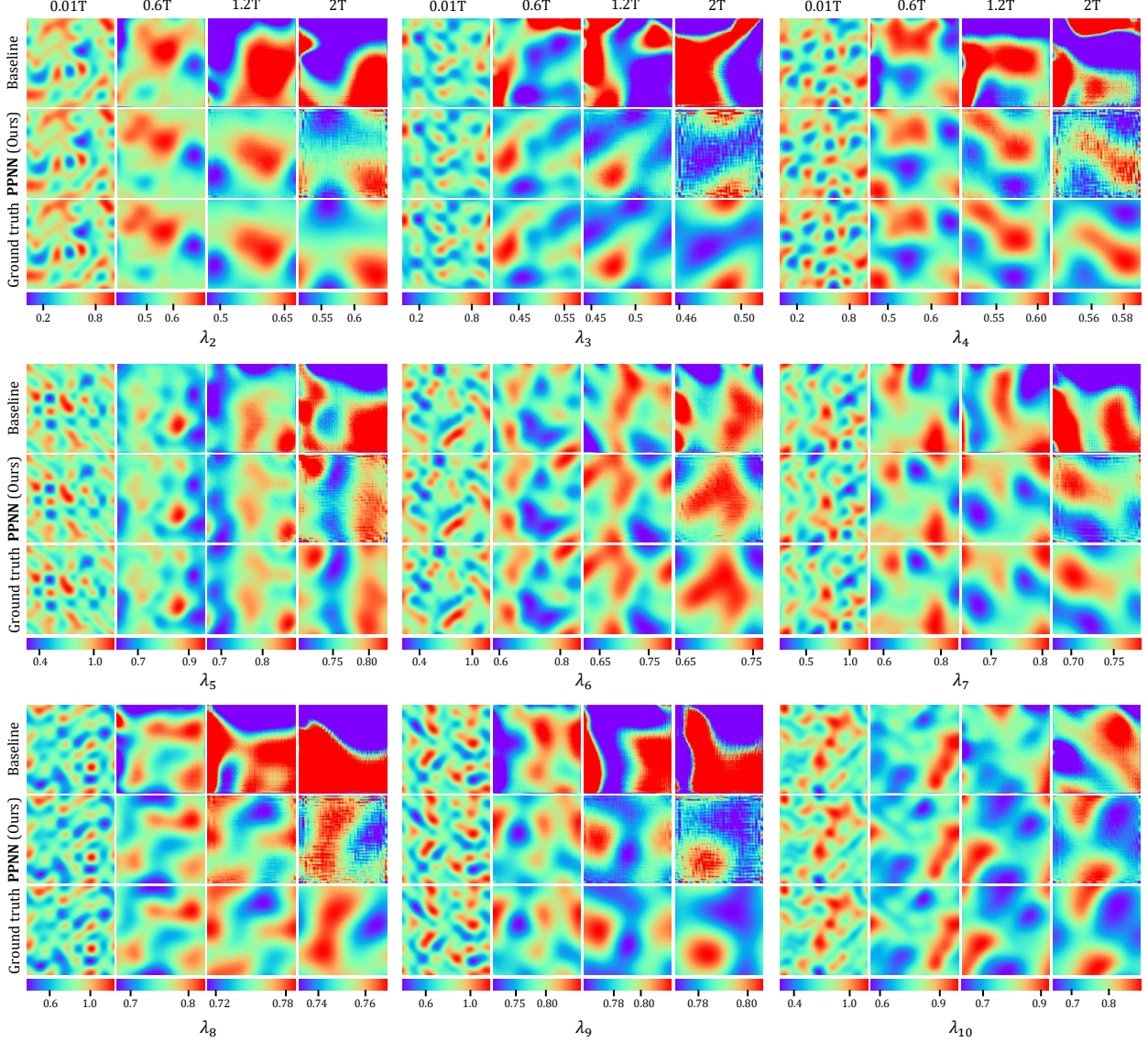


**Figure 4:** Predicted solution snapshots of reactant  $u$  for the Burgers' equations, obtained by black-box ConvResNet (baseline), and PPNN (ours); compared against ground truth. where  $\lambda_2 - \lambda_{10}$  are testing parameters, which are not in the training set.

learning step ( $t = 2T$ ). The error propagation of both models is given in Fig. 2, where the rollout errors  $\epsilon_t$  at each time step, averaged over 100 randomly selected parameters from training and testing sets, are plotted. Fig. 2e shows the averaged model rollout error evaluated on 100 training parameters, while Fig. 2f shows the error averaged on 100 randomly generated parameters, which are not used for training. As both models are only trained with the  $1T$  ( $100\Delta t$ ) time steps for each parameter in the training set, it is clear that the error of the black-box model grows rapidly once stepping into the extrapolation range  $[T, 2T]$ . The error accumulation effect of the black-box model becomes more obvious for those parameters which are not in the training set due to the poor generalizability. In contrast, the error of PPNN predictions remains surprisingly low even in the extrapolation range for both training and testing regimes, and there is nearly no error accumulation at all. In addition, the error scattering notably shrinks compared to that of the black-box model,

indicating significantly better accuracy, generalizability and robustness of the PPNN compared to the black-box baseline.

**Naiver-Stokes equations** The last case investigates the performance of PPNN to learn an unsteady fluid system exhibiting complex vortex dynamics, which is governed by the 2D parametric unsteady Naiver-Stokes (NS) equations:

$$\begin{aligned} \frac{\partial \mathbf{u}}{\partial t} + \mathbf{u} \cdot \nabla \mathbf{u} &= -\nabla p + \nu \nabla^2 \mathbf{u}, \quad t \in [0, T], \\ \nabla \cdot \mathbf{u} &= 0, \end{aligned} \tag{8}$$

where  $\mathbf{u} = [u(x, y, t), v(x, y, t)]^T \in \mathbb{R}^2$  is the velocity vector,  $p(x, y, t) \in \mathbb{R}$  is the pressure, and  $\nu = 1/Re$  represents the kinematic viscosity ( $Re$  is the Reynolds number). The NS equations are solved in a 2D rectangular domain  $(x, y) \in [0, 4] \times [0, 1]$ , where a jet with dynamically-changed jet angle is placed at the inlet. Namely, the inflow boundary is defined by a prescribed velocity profile  $\mathbf{u}(0, y, t)$ ,

$$\mathbf{u}(0, y, t) = \begin{bmatrix} u(0, y, t) \\ v(0, y, t) \end{bmatrix} = \begin{bmatrix} \exp(-50(y - y_0)^2) \\ \sin(t) \cdot \exp(-50(y - y_0)^2) \end{bmatrix} \tag{9}$$

where  $y_0$  represents the vertical position of the center of the inlet jet. The outflow boundary condition is set as pressure outlet with a reference pressure of  $p(4, y, t) = 0$ . No-slip boundary conditions are applied on the upper and lower walls. In this case, the neural network models are expected to learn the fluid dynamics with varying Reynolds number  $Re$  and jet locations  $y_0$ . Namely, a two-dimensional physical parameter vector  $\boldsymbol{\lambda} = [Re, y_0]^T$  is considered. In training set, we use five different  $Re$  evenly distributed in the range  $[2 \times 10^3, 1 \times 10^4]$  and 9 different jet locations  $y_0$  uniformly selected from 0.3 to 0.7. Figure 5a-b shows the snapshots of velocity magnitude of the NS equations at two representative testing parameters, which are not seen in the training set. To be specific,  $\boldsymbol{\lambda}_0 = [2500, 0.325]^T$  represents a relatively low Reynolds number  $Re = 2500$  with the jet located at  $y_0 = 0.325$ , while  $\boldsymbol{\lambda}_1 = [8500, 0.575]^T$  is a higher Reynolds number case ( $Re = 8500$ ) with the jet located at  $y_0 = 0.325$ . The rollout prediction results of the PPNN and baseline black-box ConvResNet are compared with the ground truth reference. Although both models can accurately capture the spatiotemporal dynamics at the beginning stage (when  $t \leq 0.4T$ ), showing good predictive performance for the unseen parameters for a short-term rollout, the predictions by the black-box model are soon overwhelmed by the noises due to the rapid error accumulation ( $t > T$ ). However, the proposed PPNN significantly outperforms the black-box baseline as it managed to provide accurate rollout predictions even at the last testing steps ( $t = 3T$ ), which extrapolate as three times long as the training range, indicating preserving the PDE structure can effectively suppress the error accumulation, which is unavoidable in most auto-regressive neural predictors. To further investigate the error propagation in time for both models, we plot the relative testing errors  $\epsilon_t$  against time in Fig. 5c-d, which are averaged over 5 randomly selected parameters in both training (Fig. 5c) and testing sets (Fig. 5d). We can clearly see that PPNN managed to maintain an extremely low rollout error in both training and extrapolation ranges, in contrast to the remarkable error accumulation in the black-box baseline results. In particular, the black-box model relative error notably grows only after a short-term model rollout and increases rapidly once it enters the extrapolation range even for testing on the training parameter set (Fig. 5c), and the errors are accumulated even faster for the testing on unseen parameters (Fig. 5d). On the contrary, our PPNN has almost no error accumulation and performs much more consistently between the training and extrapolation ranges, with significantly lower rollout errors. The results

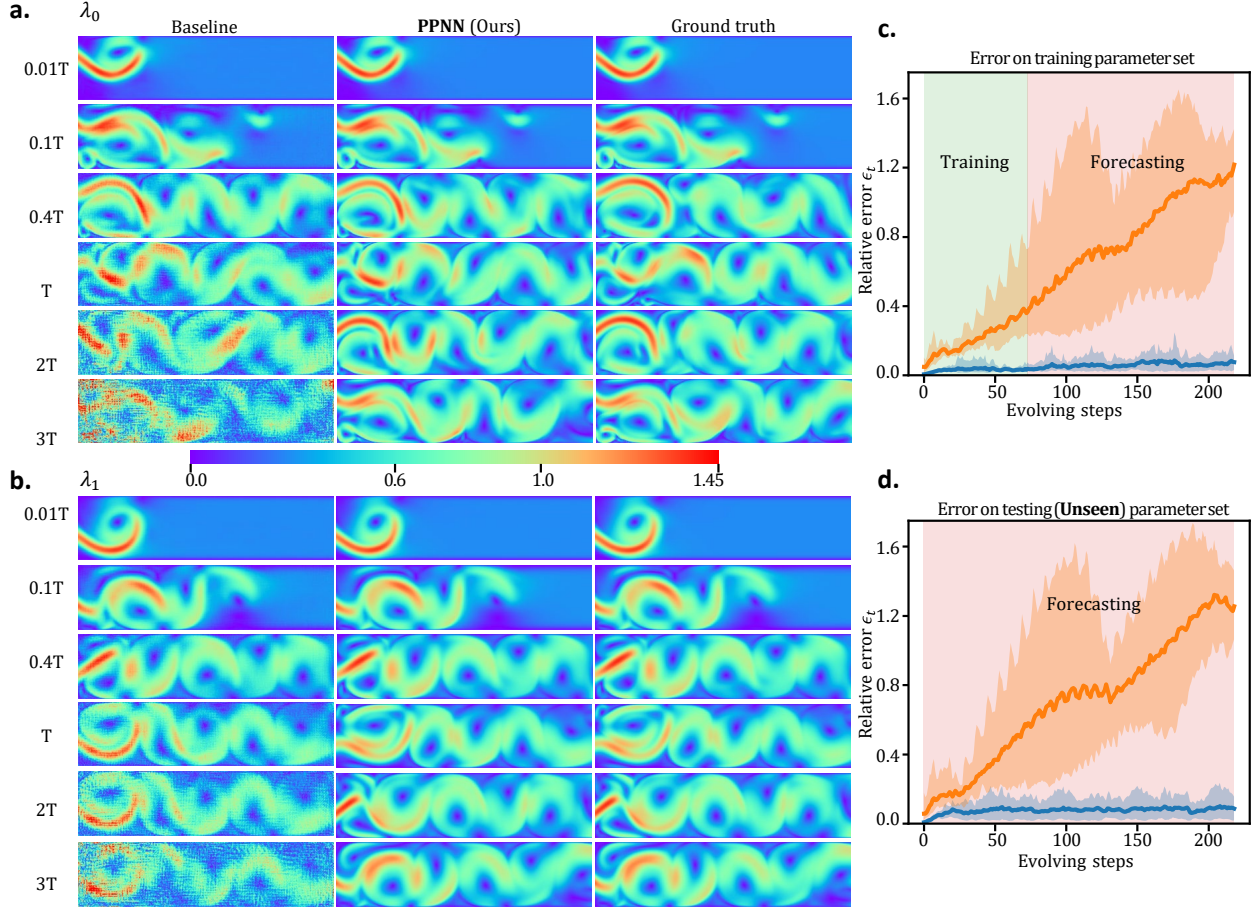


**Figure 5:** **a-b**, Predicted solution snapshots of velocity magnitude  $\|\mathbf{u}\|_2$  for the NS equations obtained by black-box ConvResNet (baseline); PPNN (Ours), compared against the ground truth (high-resolution FV simulation), where  $\lambda_0$  is ( $Re = 2500, y_0 = 0.325$ , shown in **a**), and  $\lambda_1$  is high Reynolds number ( $Re = 8500, y_0 = 0.575$ , shown in **b**). **c-d**, Relative prediction error  $\epsilon_t$  of PPNN (—) and black-box ConvResNet baseline (—) at different timesteps for the NS equation, averaged on 5 randomly sampled **(c)** training parameters and **(d)** testing (*unseen*) parameters. The shaded areas show the scattering of the relative errors over all testing trajectories.

again demonstrate outstanding predictive accuracy and generalizability of the proposed method. Besides, PPNN also shows a significantly smaller uncertainty range, indicating great robustness among different testing parameters.

### When the governing PDEs are partially known

In real-world applications, the underlying physics behind complex spatiotemporal phenomena might not be fully understood, and thus the governing equations can be incomplete, e.g., with unknown source terms, inaccurate physical parameters, or uncertain I/BCs. Such partially-known physics poses great challenges to the traditional simulation paradigm since the governing equations are partially known. Nonetheless, the incomplete prior knowledge can be well utilized in our proposed PPNN framework, where preserving partially-known governing PDE structures can still bring significant merits to data-driven spatiotemporal learning and prediction, which will be discussed in this subsection.

**Reaction diffusion equations with unknown reaction term** We first revisit the aforementioned FitzHugh–Nagumo RD equations. Here, we consider the scenario where only the diffusion phenomenon is known in the FitzHugh–Nagumo RD dynamics. Namely, the reaction source terms remain unknown and PPNN only preserves the incomplete RD equations, i.e., 2D diffusion equations,

$$\frac{\partial \mathbf{u}}{\partial t} = \gamma \nabla^2 \mathbf{u}. \quad (10)$$

All the case settings remain the same as those discussed previously. Although incomplete/inaccurate prior knowledge about the RD system is preserved, our PPNN still shows a significant advantage over the black-box baseline. Figure 6a compares the snapshots of reactant  $u$  at two randomly selected unseen parameters  $\lambda_2$  and  $\lambda_3$  predicted by black-box baseline model (first rows), PPNN with the diffusion terms preserved only (second rows), PPNN with the complete RD equation preserved (third rows), against the ground truth (fourth rows). The PPNNs preserving either complete or incomplete RD equations accurately capture the overall patterns and well agree with the reference solutions, while the black-box baseline shows notable discrepancy and large errors, particularly at  $t = 2T$ , which is the twice of the training phase length. At the last extrapolation step, the prediction results of black-box baseline show some visible noise and are less smooth compared to the results by preserving the complete RD equation, indicating that lack of the prior information on the reactive terms could slightly reduce the improvement by PPNN. Figure 6b-c shows the relative model rollout errors averaged over 100 test trajectories, which are not seen in the training set. The shaded area in the upper panel shows the error distribution range of these 100 test trajectories. Even the preserved PDEs are not complete/accurate, the mean relative error (—) remains almost the same as the PPNN with fully-known PDEs (see Fig. 2a), which is significantly lower than that of the black-box baseline (—), showing a great advantage of preserving governing equation structures even if the prior physics knowledge is imperfect. Compared to the PPNN with fully-known PDEs, the error distribution range by preserving partially-known PDEs is increased and error ensemble is more scattered, implying slightly decreased robustness. Although the envelope of the error scattering for incomplete PDEs is much larger than that of the case with fully-known PDEs, this is due to a single outlier trajectory, which can be seen in Fig. 6c. In general, the standard deviation of the error ensemble from the PPNN with partially-known PDE ( $\sigma = 1.123 \times 10^{-4}$ ) is still significantly lower than that of the black-box baseline ( $\sigma = 3.412 \times 10^{-4}$ ). In comparison, the standard deviation of errors in PPNN with fully-known PDEs over the 100 test trajectories is  $0.854 \times 10^{-4}$ .

**Naiver-Stokes equations with an unknown magnetic field** In the second case, we consider the the complex magnetic fluid dynamic system governed by Naiver-Stokes equations with an unknown magnetic field:

$$\begin{aligned} \frac{\partial \mathbf{u}}{\partial t} + \mathbf{u} \cdot \nabla \mathbf{u} &= -\nabla p + \nu \nabla^2 \mathbf{u} + \mathbf{F}, \\ \nabla \cdot \mathbf{u} &= 0, \end{aligned} \quad (11)$$

where  $\mathbf{u} = [u, v]^T$  is the velocity vector;  $p$  is the pressure; while  $\nu$  represents the kinematic viscosity. Here  $\mathbf{F} = [F_x, F_y]^T$  represents the body force introduced by a magnetic field:

$$\begin{aligned} F_x &= mH \frac{\partial H}{\partial x}, \quad F_y = mH \frac{\partial H}{\partial y} \\ H(x, y) &= \exp \left[ -8 \left( (x - L/2)^2 + (y - W/2)^2 \right) \right] \end{aligned} \quad (12)$$

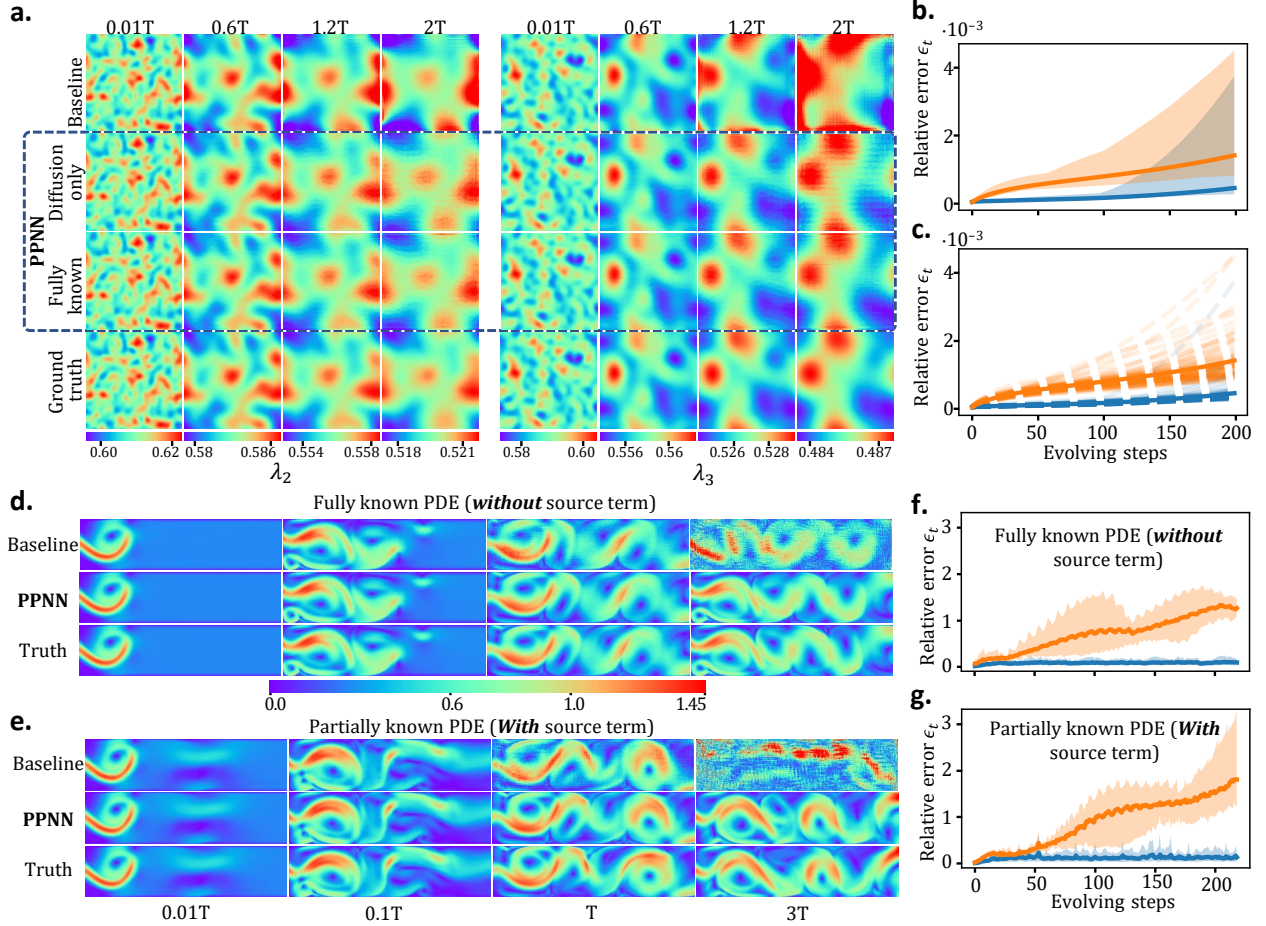


**Figure 6:** **a**, Predicted solution snapshots of  $u$  for the RD equations at different time steps and unseen parameters, obtained by black-box ConvResNet (baseline model), and PPNN (preserving diffusion terms only), and PPNN (preserving complete FitzHugh–Nagumo RD equations), compared against ground truth.  $\lambda_2$  and  $\lambda_3$  are two randomly selected testing (unseen) parameters. **b-c**, Averaged relative testing error  $\epsilon_t$  of the PPNN with incomplete PDE (—) and Black-Box ConvResNet baseline (—) for the RD dynamics evaluated on 100 randomly generated testing (unseen) parameters (same parameters as shown in Fig. 2c). Shaded areas in **b** indicate envelopes of the maximum and minimum relative errors of all testing trajectories, while the dash lines in **c** indicate the relative error of each test trajectory. **d-e**, Predicted solution snapshots of flow velocity magnitude  $\|\mathbf{u}\|_2$  obtained by black-box ConvResNet (baseline), PPNN (ours), compared against ground truth (high-resolution FV simulation) of the NS equations (upper) without and (lower) with an unknown magnetic source term. The PPNN only preserves a NS equation portion for both scenarios, which are at the same testing (unseen) parameter  $\boldsymbol{\lambda} = [9000, 0.475]^T$ , which is not in the training set. **f-g**, Relative prediction errors  $\epsilon_t$  of the PPNN (—) and black-box ConvResNet baseline (—) for the NS equation with (e) and without (f) a unknown magnetic body force, averaged on five randomly sampled unseen parameters. The shaded area shows the scattering of relative errors for all testing trajectories.

where  $m = 0.16$  is the magnetic susceptibility, and  $H$  is a time-invariant magnetic intensity. The contour of the magnitude of the body force source term is shown in the supplementary materials. In this case, the magnetic field remains unknown and PPNN only preserves the NS equation without the magnetic source term. All the other case settings remain unchanged as described in the Navier-Stokes equation case.

Similar to what we observed in the example of RD equations with the unknown reaction term, the PPNN still remains a significant advantage over the black-box baseline even by preserving an incomplete physics of the flow in a magnetic field. Fig. 6d-e, shows the velocity magnitude  $\|\mathbf{u}\|_2$

results of the flow with (Fig. 6d) or without (Fig. 6e) a magnetic field at the same testing parameter ( $\lambda = [Re = 9000, y_0 = 0.475]^T$ ), predicted by the PPNN and black-box ConvResNet, compared against the reference solution. For both scenarios, only the NS equation portion is preserved in the PPNN, i.e., the magnetic field remains unknown. Figure 6d shows the solution snapshots for the flow without the magnetic field (i.e., PPNN preserving the complete physics), while Fig. 6e shows the predictions of the flow with the magnetic field (i.e., PPNN preserving an incomplete physics). Comparing the reference solutions at upper and lower panels, the spatiotemporal patterns of the flow fields exhibit notable differences for the cases with and without magnetic fields. In both scenarios, the black-box baseline model suffers from the long-term model rollout, particularly for the flow within the magnetic field, the black-box baseline completely fails to capture the physics when  $t > 2T$ . In both scenarios, the PPNN remarkably outperforms the black-box baseline. In particular at the last time step  $t = 3T$ , which is three times the training phase length, the black-box predictions are totally overwhelmed by noise, while our PPNN predictions still agree with the reference very well. Compared to the case preserving the complete physics (Fig. 6d), a slight deviation from the reference solution can be observed in the PPNN predictions of the flow with an unknown magnetic field (Fig. 6e), indicating that incomplete prior knowledge could slightly affect the PPNN performance negatively. Nonetheless, preserving the partially-known PDE structure still brings significant merit. The error propagation is shown in Fig. 6f-g. The relative model rollout errors are averaged over 5 randomly selected unseen parameters for the systems with (Fig. 6f) and without (Fig. 6g) the magnetic field. Comparing to the PPNN with completely-known PDEs, the PPNN preserving incomplete/inaccurate prior knowledge does show a slight increment in the mean relative error  $\epsilon_t$  as well as the error scattering, which implies a slight decrease in the robustness. However, the significant advantage over the black-box baseline remains, and almost no error accumulation is observed in PPNN for both scenarios.

## Training and inference cost

We have demonstrated that the proposed PPNN significantly improves the accuracy, generalizability, and robustness of next-step neural predictors by preserving the mathematical structure of the governing PDEs. Since the PPNN has a more complex network structure than the black-box baseline, it is worthwhile to discuss the training and inference costs of the PPNN and its comparison with the corresponding black-box baseline and the reference numerical solvers.

**Training cost** As shown in Fig. 7a, the averaged relative (rollout) prediction error  $\epsilon_T$  on  $n$  testing parameters  $\lambda$  at the last time step  $T$  in the training process ( $n = 8$  in RD,  $n = 6$  in Burgers,  $n = 5$  in NS). For all the cases, PPNN features a significantly (orders of magnitude) lower error than the black-box model from a very early training stage. This means that, to achieve the same (if not higher) level of accuracy, our PPNN requires significantly less training cost compared to the black-box baseline. In addition, under the same training budget, the PPNN is much more accurate than the black-box baseline, demonstrating the merit of PPNN by leveraging the prior knowledge for network architecture design.

**Inference cost** The inference costs of different neural networks and numerical solvers on the three testing cases (see section [When the governing PDEs are fully known](#)) with the model rollout length of  $T$  are summarized in Fig. 7b. Due to the fast inference speed of neural networks, both next-step neural models show significant speedup compared to the high-fidelity numerical solvers. In particular, the speedup by the PPNN varies from  $10\times$  to  $60\times$  without notably sacrificing the prediction accuracy. Such speedup will become more tremendous considering a longer model rollout

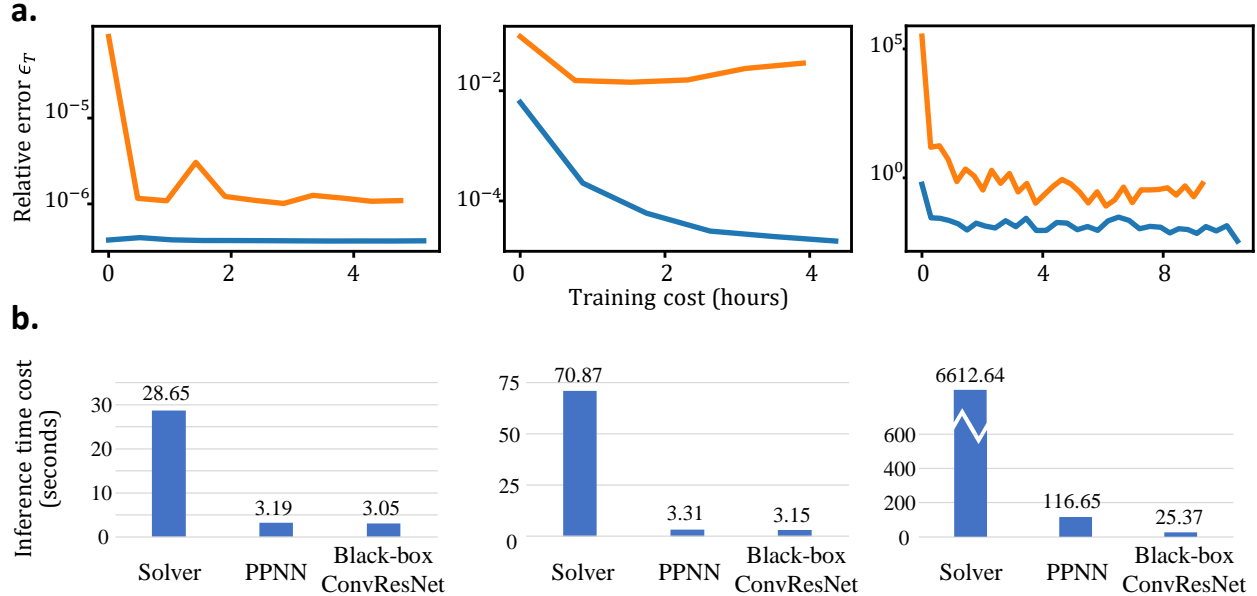


**Figure 7:** **a**, Averaged relative test error at the last time step  $\epsilon_T$  of PPNN (—) and black-box ConvResNet (—) in training process of different cases in section [When the governing PDEs are fully known](#) (from left to right, RD, Burgers, and NS). **b**, inference time cost of numerical solver, PPNN and black-box ConvResNet in the case RD, Burgers, and NS (from left to right). The RD and Burgers cases are inferred (simulated) on a NVIDIA RTX 3070 GPU and the time is measured for infer/simulate 10 trajectories for 200 time steps. The NS case is inferred/simulated on a single of Intel Xeon Gold 6138 CPU and the time is measured for infer/simulate 1 trajectory for 219 time steps.

and enormous repeated model queries on a large number of different parameter settings, which are commonly required in many-query applications such as optimization design, inverse problems, and uncertainty quantification. Note that all models are compared on the same hardware (GPU or CPU) to eliminate the difference introduced by hardware. However, as most legacy numerical solvers can only run on CPUs, the speedup by neural models can be much more significant if they leverage massive GPU parallelism. Admittedly, adding the PDE-preserving part inevitably increases the inference cost compared to the black-box baseline, but the huge performance improvement by doing so outweighs the slight computational overhead, as demonstrated in section [When the governing PDEs are fully known](#). We have to point out that the computation of the PDE-preserving portion is not fully optimized, particularly in the NS case, where low-speed I/O interactions reduce the overall speedup ratio compared to the numerical solver based on the mature CFD platform OpenFOAM. Further performance improvements are expected by customized code optimizations in future work.

## Relationship between the PDE-preserving Portion and Numerical Solvers

The advantages of the proposed PPNN over the pure black-box baseline mainly come from “baking” the prior knowledge into the network architecture. As discussed above, the mathematical structures of the governing physics are encoded into the PPNN based on the relationship between neural network structures and differential equations. From the numerical modeling perspective, if our understanding of the underlying physics is complete and accurate (i.e., complete governing PDEs are available), the PDE-preserving portion in PPNN can be interpreted as a numerical solver with the explicit forward Euler scheme defined on a coarse mesh. For simplicity, we here refer to this numerical solver derived from the fully-known PDE preserving part as the “coarse solver”. It is interesting to see how well it performs by the coarse solver only when governing equations and

IC/BCs are fully known.

We use the NS case as an example. Fig. 8b shows the magnitude of velocity  $\|\mathbf{u}\|_2$  predicted by the PPNN, black-box ConvResNet and coarse solver, respectively, compared against the reference solution. Two representative testing parameters are studied here, one is at a lower Reynolds number  $Re = 2500, y_0 = 0.325$  (Fig. 8b left), and the other is at a higher Reynolds number  $Re = 9000, y_0 = 0.475$  ( Fig. 8b right). It is clear that the predictions by the coarse solver notably deviate from the reference solution from  $0.4T$ , and most vortices are damped out due to the coarse spatial discretization. This becomes worse in the higher Reynolds number scenario, where the coarse solver predicted flow field is unphysical at  $0.1T$  and the simulation completely diverged at  $t = 1.16T$ , because of the large learning timestep making traditional numerical solvers fail to satisfy the stability constraint.

As shown in the error propagation curves in Fig. 8a, the coarse solver has large prediction errors over the testing parameter set from the very beginning, which is much higher than that of the black-box data-driven baseline. Since several of the testing trajectories by the coarse solver diverges quickly after 70 evolving steps, the error propagation curve stops.

This figure again empirically demonstrates that the PPNN structure not only overcomes the error accumulation problem in black-box methods, but also significantly outperforms numerical solvers by simply coarsen the spatiotemporal grids. On the other hand, for those trajectories that do not diverge, the coarse solver’s relative errors are limited to a certain level, which is in contrast to black-box, data-driven methods where the error constantly grows due to the error accumulation. This phenomenon implies that preserving PDEs plays a critical role in addressing the issue of error accumulation, which does not simply provide a rough estimation of the next step, but carries underlying physics information that guides the longer-term prediction.

## Comparison with existing SOTA methods for neural operator learning

The backbone of the proposed PPNN method is a next-step auto-regressive model, which learns the transition dynamics of a spatiotemporal process, by mapping the solution fields from previous time steps to the next ones, and the whole trajectory prediction is obtained by rolling out the learned transition model autoregressively. Since the PPNN prediction is also conditioned on parameters  $\lambda$ , the proposed model can be interpreted as learning an operator  $\mathcal{G}$  in a discrete manner,

$$\mathcal{G} : \mathbf{u}(\boldsymbol{\xi}; \lambda) \mapsto \mathcal{G}[\mathbf{u}(\boldsymbol{\xi}; \lambda)], \tag{13}$$

where  $\boldsymbol{\xi} = [\mathbf{x}, t]$  represents spatial and temporal coordinates and  $\mathbf{u} \in \mathbb{R}^n$  is the  $n$ -dimensional state variable. In addition to the auto-regressive formulation, one can directly learn the operator  $\mathcal{G}$  using deep neural networks in a continuous manner, generally referred to as *neural operators*. In the past few years, several continuous neural operator learning methods have been proposed, e.g., DeepONet [25, 62] and Fourier Neural Operator (FNO) [26]. Although many of them have shown great success for a handful of PDE-governed systems, it remains unclear how these methods perform compared to our proposed PPNN on the challenging scenarios studied in this work,

- Problems with high-dimensional parameter space, i.e.,  $\lambda \in \mathbb{R}^d, d \gg 1$ .
- Limited training data for good generalizability in parameter space and temporal domain.

Therefore, we conduct a comprehensive comparison of PPNN with existing state-of-the-art (SOTA) neural operators, including physics-informed neural network (PINN) [12], DeepONet [25, 62], and Fourier Neural Operator (FNO) [26], on one of the previous test cases, [Viscous Burgers’ equation](#), where the PDE is fully known. (Strictly speaking, original PINN by Rassi et al. [12] is not an

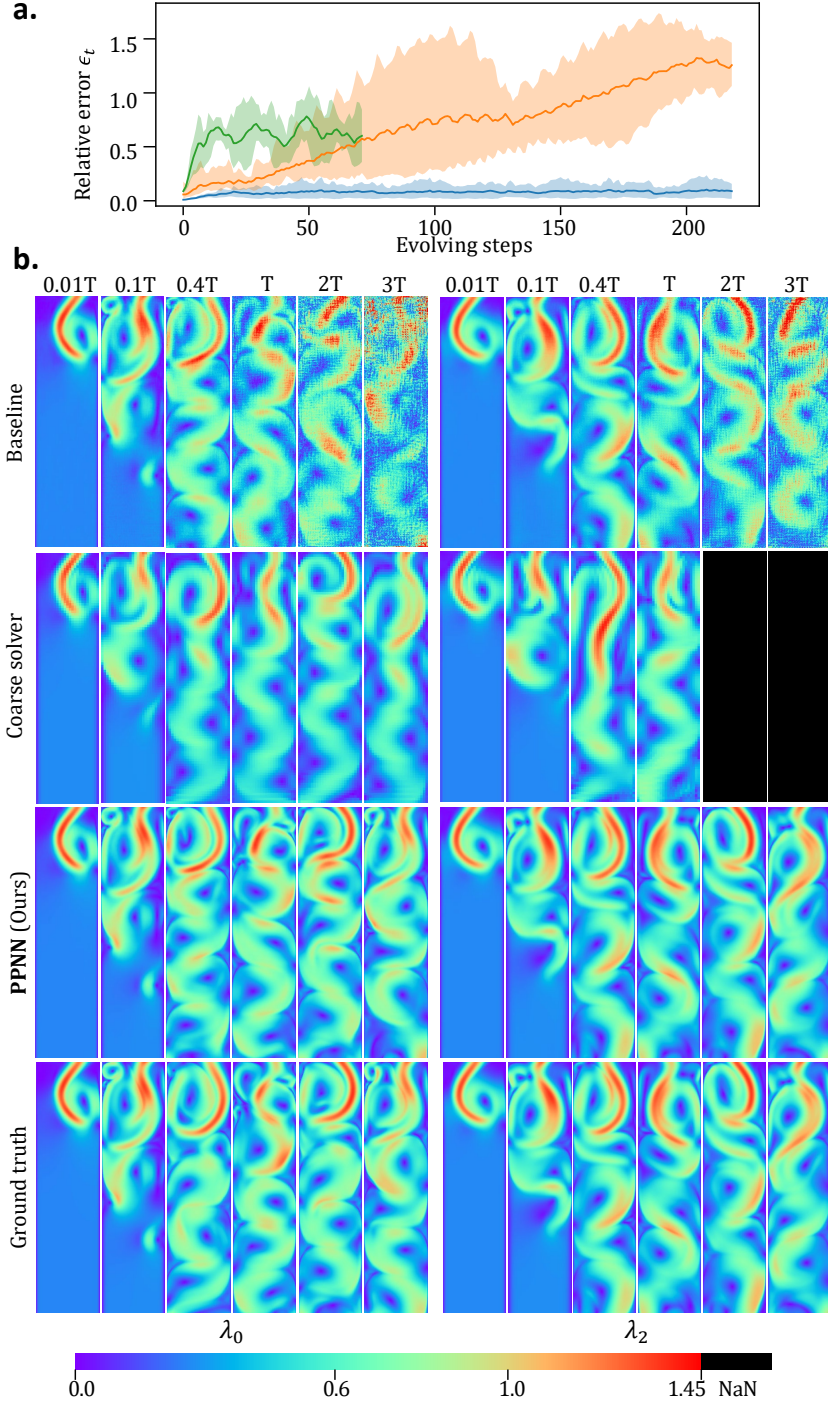


**Figure 8:** **a**, Relative error (the upper part) at different time steps of PPNN (—), Black-Box neural network (—) and the coarse solver (—) compared to the ground truth results obtained by icoFoam on a fine mesh. The relative error is an averaged value of 5 test trajectories with randomly sampled parameters, these parameters are not in the training set. The shaded area shows the maximum and minimum relative error of these testing trajectories. In coarse solver, 2 of the testing trajectories diverged (NaN) at the 72<sup>nd</sup> step thus the curve (—) stops at the 71<sup>st</sup> step. **b**, The contours (the lower part) show predicted solution snapshots of velocity magnitude  $\|u\|_2$  for the NS equations, obtained by black-box ConvResNet (baseline), PDE-preserving part only (coarse solver), and PPNN (ours); compared against ground truth (high-resolution FV simulation), where  $\lambda_0 = [2500, 0.325]^T$  and  $\lambda_2 = [9000, 0.475]^T$ , which are unseen in the training set. The black color indicates NaN, i.e., solution blow up.

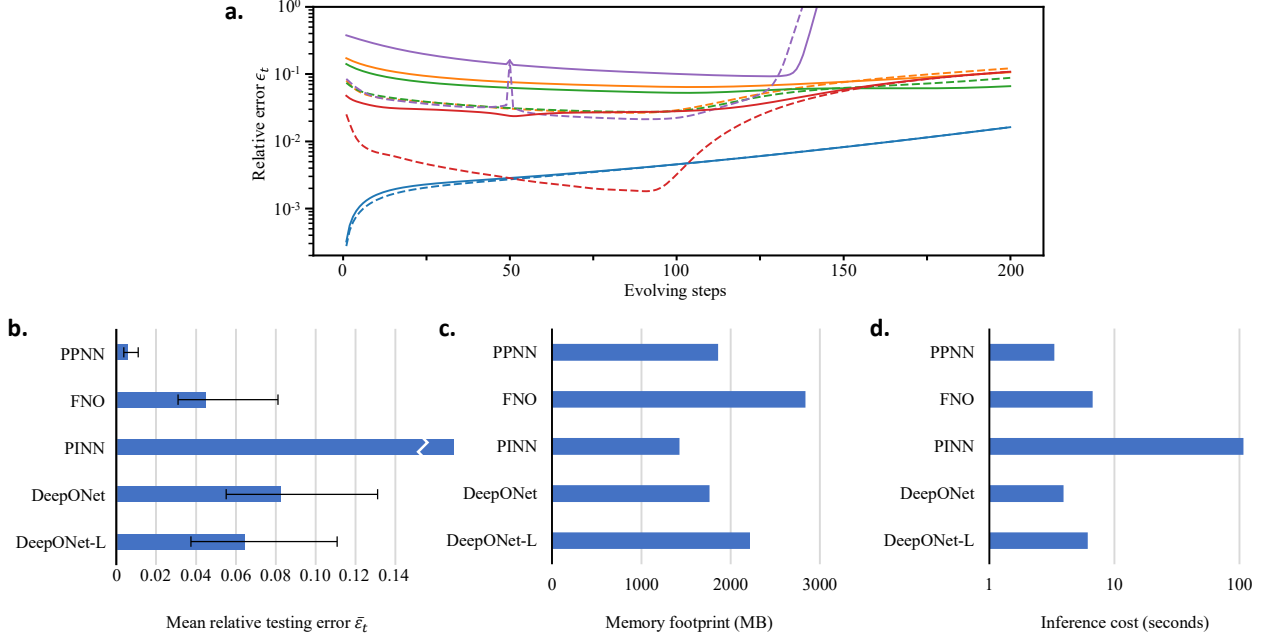


**Figure 9:** **a.** Comparison of the relative error  $\epsilon_t$  of the PINN (—), DeepONet (—), DeepONet-L (—), FNO (—), and PPNN (—) of the velocity  $\mathbf{u}$  in the viscous Burgers’ equation evaluated on 100 randomly generated testing (unseen) parameters (solid lines), and 100 randomly selected training parameters (dashed lines). Only the first 100 time steps are used for training. Note that the y axis is in log scale. **b.** Relative testing error averaged over all testing parameters and time steps  $\bar{\epsilon}_t$  with error bar. Note that PINN has a much higher error than the other models which cannot be completely shown in this figure. **c.** The memory footprint of different methods when testing 10 trajectories. **d.** The inference cost of testing 10 trajectories on a NVIDIA RTX 3070 GPU.

operator learner, but can be easily extended to achieving so by augmenting the network input layer with the parameter dimension, as shown in [13].) For a fair comparison, the problem setting and training data remain the same for all the methods and the number of trainable parameters of each models are comparable (PINN: 1.94M parameters; DeepONet: 1.51M parameters<sup>1</sup>; PPNN: 1.56M parameters). Except for FNO<sup>2</sup>, which has 0.58M trainable parameters due to the spatial Fourier transformation in FNO is too memory-hungry for a larger model to fit into the GPU used for training (RTX A6000 48GB RAM). Besides, we also include a DeepONet with significantly more trainable parameters (79.19M) to show the highest possible performance DeepONet would achieve, which is named as DeepONet-L. Note that since some of these models’ original forms cannot be directly applied to learn parametric spatiotemporal dynamics in multi-variable settings, necessary modifications and improvement has been made. The implementation details and hyper-parameters of these models are provided in the supplementary materials.

**Predictive performance comparison** All the models are used to predict the spatiotemporal dynamics of 100 randomly generated initial fields which are not seen in training. The relative prediction errors  $\epsilon_t$  of the existing SOTA neural operators and PPNN are compared in Fig. 9.

<sup>1</sup>We used two separate but identical neural networks to learn the two components  $u_x, u_y$  of velocity  $\mathbf{u}$  respectively; each network contains 0.755M trainable parameters

<sup>2</sup>FNO could be formulated either as a continuous operator or as an autoregressive model. Here we show the performance of the continuous FNO. The performance of autoregressive FNO (named as aFNO) is shown in the supplementary materials, which is slightly better compared to continuous FNO in terms of testing error with unseen parameters.

As shown in Fig. 9a and 9b, PPNN significantly outperforms all the other SOTA baselines for all the time steps in both training and testing parameter regimes. All the existing SOTA neural operators have much higher prediction errors (several orders of magnitude higher) compared to PPNN, especially when entering the extrapolation range (after 100 time steps), where the error grows rapidly. In contrast, the relative error of PPNN predictions remains very low ( $10^{-3}$ ) and barely accumulated evolving with time. The prediction errors of most continuous neural operators do not grow monotonically since their predictions do not rely on auto-regressive model rollout and thus does not have error accumulation issue. However, the overall accuracy of all continuous neural operators (particularly in extrapolation range) is much lower than that of PPNN. Besides, PPNN exhibits a much smaller error scattering over different testing samples, indicating remarkably higher robustness compared to existing SOTA methods. All of these observations suggest the obvious superiority of the PPNN in terms of extrapolability in time. The comparison of the generalizability in parameter space of all methods is shown in Fig. 9a, where the dashed lines represent the averaged testing errors on the training parameter set, while the solid lines indicate the errors on the testing parameter set. It is clear that all the continuous neural operators have a significantly higher prediction error on the testing set than that on the training set, while the PPNN’s prediction errors are almost the same on both the testing and training sets, which are much lower than all the other methods, indicating a much better generalizability. It is worth mentioning that the notable overfitting issue is observed in DeepONet with increased trainable parameters, i.e., DeepONet-L. It can be seen that although the prediction errors of DeepONet-L and FNO are relatively lower on training parameter sets and interpolation regimes, they rapidly increase when stepping into extrapolation ranges and unseen parameter regimes.

**Cost comparison** Figures 9c and 9d show the time cost and memory footprint in the inference phase. Even compared to the fastest baseline DeepONet<sup>3</sup>, PPNN is still about 20% faster and the memory footprint of PPNN is very close to the smallest model: DeepONet<sup>4</sup>. It should be noted that all the models, including our PPNN are exhaustively fine-tuned. Although carefully tuning hyperparameters may further improve the performance of each model, issues such as generalizability or robustness presented above cannot be addressed by hyperparameter tuning.

## DISCUSSION

In this work, we proposed a novel physics-inspired deep learning architecture, PDE-preserved neural network (PPNN), aiming to learn parametric spatiotemporal physics, where the (partially) known governing PDE structures are preserved via convolutional residual connection blocks in a multi-resolution setting. The PDE-preserving ConvResNet blocks together with trainable ConvResNet blocks in an encoding-decoding manner bring the PPNN significant advantages in long-term model rollout accuracy, spatiotemporal/parameter generalizability, and training efficiency. The effectiveness and merit have been demonstrated over a handful of challenging spatiotemporal prediction tasks, including the FitzHugh–Nagumo reaction diffusion equations, viscous Burgers equations and Navier-Stokes equations, compared to the existing state-of-the-art baselines, including Mesh-GraphNet, PINN, DeepONet, and FNO. The proposed PPNN shows excellent predictive accuracy

<sup>3</sup>The inference time of PINN is measured for the inference-optimized variants of the original models, which are significantly faster than the original form used for training.

<sup>4</sup>The time cost and memory footprint measured of PINN is the amount required for inferring a single row of the target mesh at a time. Inferring the whole field requires much more memory, which exceeds the inference device’s capacity.

in testing regimes and remarkably low error-accumulation effect for long-term model rollout in time, even if the preserved physics is incomplete or inaccurate. Admittedly, very mild error accumulation can still be observed when extrapolating to a very long duration, which is due to the one-step predicting formulation of the current PPNN. This can be further improved by utilizing sequence network structures, e.g., recurrent neural networks and temporal attention schemes, which are capable of leveraging multiple-step solution information to learn higher-order-accurate time-stepping schemes that are numerically stable. Finally, the discussion on the inference and training costs shows the great potential of the proposed model to serve as a reliable and efficient surrogate model for spatiotemporal dynamics in many applications that require repeated model queries, e.g., design optimization, data assimilation, uncertainty quantification, and inverse problems. In general, this work explored a novel direction of leveraging physics-induced bias in scientific machine/deep learning and showcased how to use physical prior knowledge to inform the learning architecture design, shedding new light on physics-informed deep learning from a different aspect. Although this work is limited to structured data for ease of implementation, the concept of “preserving PDE structures” can be further extended to unstructured data for problems with complex geometries, by leveraging the relationship between graph neural networks and PDEs discretized by finite volume/element methods.

## METHODS

### Problem formulation

We are interested in predictive modeling of physical systems with spatiotemporal dynamics, which can be described by a set of parametric coupled PDEs in the general form,

$$\frac{\partial \mathbf{u}}{\partial t} + \mathcal{F} \left[ \mathbf{u}, \mathbf{u}^2, \dots, \nabla_{\mathbf{x}} \mathbf{u}, \nabla_{\mathbf{x}}^2 \mathbf{u}, \nabla_{\mathbf{x}} \mathbf{u} \cdot \mathbf{u}, \dots; \boldsymbol{\lambda} \right] = \mathbf{0}, \quad \mathbf{x}, t \in \Omega \times [0, T], \boldsymbol{\lambda} \in \mathbb{R}^d, \quad (14a)$$

$$\mathcal{I} \left[ \mathbf{x}, \mathbf{u}, \nabla_{\mathbf{x}}^2 \mathbf{u}, \nabla_{\mathbf{x}} \mathbf{u} \cdot \mathbf{u}; \boldsymbol{\lambda} \right] = \mathbf{0}, \quad \mathbf{x} \in \Omega, t = 0, \boldsymbol{\lambda} \in \mathbb{R}^d, \quad (14b)$$

$$\mathcal{B} \left[ t, \mathbf{x}, \mathbf{u}, \nabla_{\mathbf{x}}^2 \mathbf{u}, \nabla_{\mathbf{x}} \mathbf{u} \cdot \mathbf{u}; \boldsymbol{\lambda} \right] = \mathbf{0}, \quad \mathbf{x}, t \in \partial\Omega \times [0, T], \boldsymbol{\lambda} \in \mathbb{R}^d, \quad (14c)$$

where  $\mathbf{u} = \mathbf{u}(\mathbf{x}, t; \boldsymbol{\lambda}) \in \mathbb{R}^n$  is the  $n$ -dimensional state variable;  $t$  denotes time and  $\mathbf{x} \in \Omega$  specifies the space;  $\mathcal{F}[\cdot]$  is a complex nonlinear functional governing the physics, while differential operators  $\mathcal{I}[\cdot]$  and  $\mathcal{B}[\cdot]$  describe the initial and boundary conditions (I/BCs) of the system, respectively;  $\boldsymbol{\lambda} \in \mathbb{R}^d$  is a  $d$ -dimensional vector, representing physical/modeling parameters in the governing PDEs and/or I/BCs. Solving this parametric spatiotemporal PDE system typically relies on traditional FD/FV/FE methods, which are computationally expensive in most cases. This is due to the spatiotemporal discretization of the PDEs into a high-dimensional algebraic system, making the numerical simulation time-consuming, particularly considering that a tiny step is often required for the time integration to satisfy the numerical stability constraint. Moreover, as the system solution  $\mathbf{u}(\mathbf{x}, t; \boldsymbol{\lambda})$  is parameter-dependent, we have to start over and conduct the entire simulation given a new parameter  $\boldsymbol{\lambda}$ , making it infeasible for application scenarios that require many model queries, e.g., parameter inference, optimization, and uncertainty quantification. Therefore, our objective is to develop a data-driven neural solver for rapid spatiotemporal prediction, enabled by efficient time-stepping with coarse-gaining and fast inference speed of neural networks. In particular, this study focuses on the learning architecture design by preserving known PDE structures for improving the robustness, stability, and generalizability of data-driven auto-regressive predicting models.

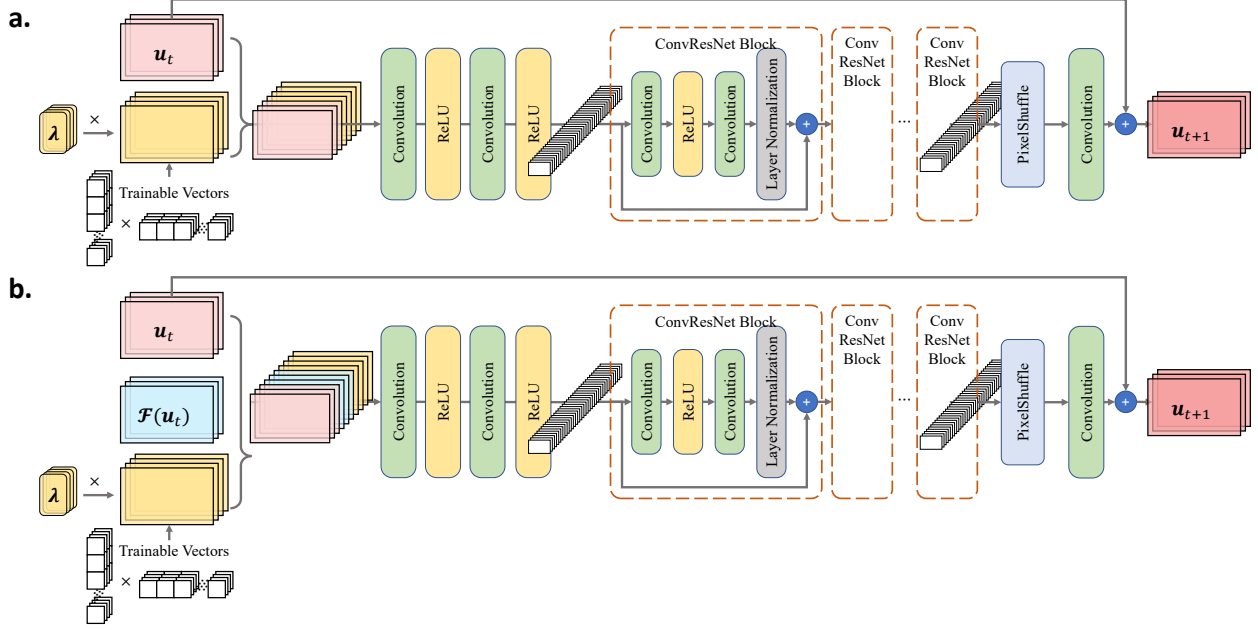


**Figure 10:** **a**, Network architecture of the baseline black-box ConvResNet-based next-step model. **b**, Network architecture of the trainable portion of PPNN. The only difference between them is trainable portion of PPNN has an extra input variable  $\mathcal{F}(\mathbf{u}_t)$ , provided by the PDE-preserving portion of PPNN.

## Next-step prediction models based on convolutional ResNets

The next-step DNN predictors are commonly used for emulating spatiotemporal dynamics in an autoregressive manner,

$$\mathbf{u}_t = f_{\theta}(\mathbf{u}_{t-1}, \lambda \mid \theta), \quad (15)$$

where the state solution  $\mathbf{u}_t$  at time step  $t$  is approximated by a neural network function  $f_{\theta} : \mathbb{R}^n \times \mathbb{R}^d \rightarrow \mathbb{R}^n$ , taking the previous state  $\mathbf{u}_{t-1}$  and physical parameters  $\lambda$  as the input features. The function  $f_{\theta}(\cdot \mid \theta)$  is parameterized by trainable weight vector  $\theta$  that can be optimized based on training labels. Once the model is fully trained, it can be used to predict spatiotemporal dynamics by autoregressive model rollouts given only the initial condition  $\mathbf{u}_0$  and a specific set of physical parameters  $\lambda$ . In general, the next-step model is built based on residual network (ResNet) blocks, which have recently improved the state-of-the-art (SOTA) in many benchmarks learning tasks [9]. Given the input features  $\mathbf{z}_0$ , a ResNet block with  $N$  layers outputs  $\mathbf{z}_N$  as,

$$\mathbf{z}_{j+1} = \mathbf{z}_j + f^{(j)}(\mathbf{z}_j \mid \theta^{(j)}), \quad j = 0, \dots, N-1, \quad (16)$$

where  $f^{(j)}$  represents the generic neural network function of  $j^{\text{th}}$  layer and  $\theta^{(j)}$  are corresponding weights. For end-to-end spatiotemporal learning,  $f^{(j)}$  are often formulated by (graph) convolutional neural networks with trainable convolution stencils and biases. In a ResNet block, the dimension of the feature vectors (i.e., the image resolution and the number of channels) should remain the same across all layers. The ResNet-based next-step models have been demonstrated powerful and effective for predicting complex spatiotemporal physics. One of the examples is the MeshGraphNet [9], which is a GNN-based ResNets and shows the SOTA performance in spatiotemporal learning with unstructured mesh data.

In this work, as we limit ourselves to structured data within regular domains, a CNN variant of the MeshGraphNet, Convolutional ResNet (ConvResNet)-based next-step model, is used as the

baseline black-box model in this work, whose network structure is shown in Fig. 10a. The ConvResNet takes the previous state and physical parameters as the input and predicts the next-step state using a residual connection across the entire hidden ConvResNet layers after a pixel shuffle layer. The hidden layers consist of several ConvResNet blocks, constructed based on standard convolution layers with residual connections and ReLU activation functions, followed by layer normalization. To learn the dependence of physical parameters  $\boldsymbol{\lambda}$ , each scalar component of the physical parameter vector is multiplied by a trainable matrix, which is obtained by vector multiplication of trainable weight vectors.

## Neural network architecture and differential equations

Recent studies have shown the relationship between DNN architectures and differential equations: ResNets can be interpreted as discretized forms of ODEs/PDEs, while differential equations can be treated as a continuous interpretation of ResNet blocks with infinite depth.

**Residual connections and ODEs** As discussed in [44, 50], the residual connection as defined in Eq. 16 can be seen as a forward Euler discretization of a ODE,

$$\frac{\partial \mathbf{z}(t)}{\partial t} = F(\mathbf{z}(t) | \boldsymbol{\theta}(t)), \quad \text{for } t \in (0, T], \quad (17)$$

where  $\mathbf{z}(t=0) = \mathbf{z}_0$  and  $T$  is total time. In ResNets, a fixed time step size of  $\Delta t = 1$  is set for the entire time span and  $N \cdot \Delta t = T$ . Namely, the depth of the residual connection (i.e., the number of layers in a ResNet block) can be controlled by changing the total time  $T$ . On the other hand, an ODE as given by Eq. 17 can be interpreted as a continuous ResNet block with infinite number of layers (i.e., infinite depth). Based on this observation, the classic ResNet structure can be extended by discretizing an ODE using different time-stepping schemes (e.g., Euler, Runge-Kutta, leapfrog, etc.). Moreover, we can also define a residual connection block by directly coupling a differentiable ODE solver with a multi-layer perception (MLP) representing  $F(\cdot)$ , where the hybrid ODE-MLP is trained as a whole differentiable program using back-propagation, which is known as a neural-ODE block [50].

**Convolution operations and PDEs** In the neuralODE, MLP is used to define  $F(\cdot)$ , which, however, can be any neural network structure in a general setting. When dealing with structured data (e.g., images, videos, physical fields), the features  $\mathbf{z}(t, \mathbf{x})$  can be seen as spatial fields, and convolution operations are often used to construct a CNN-based  $F(\cdot)$ . A profound relationship between convolutions and differentiations has been presented in [45, 63, 64]. Following the deep learning convention, a 2D convolution is defined as,

$$\text{conv}(\mathbf{z}, h^{(\theta)}) = \int \mathbf{z}(\mathbf{x}' - \mathbf{x}) h^{(\theta)}(\mathbf{x}) d\mathbf{x}, \quad (18)$$

where  $h$  represent convolution kernel parameterized by  $\boldsymbol{\theta}$ . Based on the order of sum rules, the kernel  $h$  can be designed to approximate any differential operator with prescribed order of accuracy [65], and thus the convolution in Eq. 18 can be expressed as [49],

$$\text{conv}(\mathbf{z}, h^{(\theta)}) = \mathcal{D} \left[ \mathbf{u}, \dots, \nabla_{\mathbf{x}} \mathbf{u}, \nabla_{\mathbf{x}}^2 \mathbf{u}, \nabla_{\mathbf{x}} \mathbf{u} \cdot \mathbf{u}, \dots; \boldsymbol{\theta} \right], \quad (19)$$

where  $\mathcal{D}$  is a discrete differential operator based FD/FV/FE methods. For example, from the point of view of FDM, convolution filters can be seen as the finite difference stencils of certain can

be interpreted as the discrete forms of certain PDEs, and thus the PDEs can be used to inform ConvResNet architecture design.

## Multi-resolution PDE-preserved Neural Network (PPNN) architecture

It is well known that auto-regressive models suffer from error accumulation, which is particularly severe for the next-step formulation. Although remedies such as using training noises [66] or sequence models [10] have been explored, the error accumulation issue cannot be easily mitigated, and the model usually fails to operate in a long-span rollout. Inspired by the relationship between network architectures and differential equations, we *hypothesize* that the performance of an auto-regressive ConvResNet model for spatiotemporal learning can be significantly improved if the network is constructed by preserving (partially) known governing physics (i.e., PDEs) of the spatiotemporal dynamics. Therefore, we propose a multi-resolution PDE-preserved neural network (PPNN) framework, where the discrete governing PDEs are preserved in residual connection blocks using grids with multiple resolutions.

As shown in Fig. 1, the PPNN has the same backbone ResNet structure as the black-box next-step baseline model, where a residual connection is applied across the entire hidden ConvResNet layers. The hidden ConvResNet consists of two portions: PDE-preserving ConvRes layers and trainable ConvRes layers, coupled in an encoding-decoding manner. In the PDE-preserving portion, the ConvRes connection is constructed based on the convolution operators defined by the discrete differential operators of the governing PDEs using finite-difference stencils. The preserved-PDE ConvRes layers are operated on low-resolution grids by taking in the bilinearly-downsampled input solution fields, which improves the model rollout stability with large evolving steps, meanwhile reducing the cost overhead during the model inference. The trainable portion takes the high-resolution solution fields as the input and contains a few classic ConvResNet blocks. For a fair comparison, the network architecture of the trainable portion is exactly the same as that of the black-box ConvResNet baseline, except that the trainable portion of PPNN takes the output of the PDE-preserving portion (see Fig. 10). The PDE-preserving part and trainable part are connected via bi-cubic up-sampling operation. Note that a smaller time step  $\Delta t'$  can be used within the PDE-preserving portion via inner-iteration to stabilize model rollout. In general, the combination of the two portions can be seen as a new ConResNet architecture that preserves the mathematical structure of the underlying physics behind the spatiotemporal dynamics to be modeled.

## Data availability

All the used datasets in this study will be openly available on GitHub at <https://github.com/Jianxun-Wang/PPNN> upon publication.

## Code availability

All the source codes to reproduce the results in this study will be openly available on GitHub at <https://github.com/Jianxun-Wang/PPNN> upon publication.

## References

- [1] Hugo FS Lui and William R Wolf. Construction of reduced-order models for fluid flows using deep feedforward neural networks. *Journal of Fluid Mechanics*, 872:963–994, 2019.

- [2] Omer San, Romit Maulik, and Mansoor Ahmed. An artificial neural network framework for reduced order modeling of transient flows. *Communications in Nonlinear Science and Numerical Simulation*, 77:271–287, 2019.
- [3] Han Gao, Jian-Xun Wang, and Matthew J Zahr. Non-intrusive model reduction of large-scale, nonlinear dynamical systems using deep learning. *Physica D: Nonlinear Phenomena*, 412:132614, 2020.
- [4] Stefania Fresca and Andrea Manzoni. Pod-dl-rom: enhancing deep learning-based reduced order models for nonlinear parametrized pdes by proper orthogonal decomposition. *Computer Methods in Applied Mechanics and Engineering*, 388:114181, 2022.
- [5] Takaaki Murata, Kai Fukami, and Koji Fukagata. Nonlinear mode decomposition with convolutional neural networks for fluid dynamics. *Journal of Fluid Mechanics*, 882, 2020.
- [6] Arvind T Mohan, Dima Tretiak, Misha Chertkov, and Daniel Livescu. Spatio-temporal deep learning models of 3d turbulence with physics informed diagnostics. *Journal of Turbulence*, 21(9-10):484–524, 2020.
- [7] Romit Maulik, Bethany Lusch, and Prasanna Balaprakash. Reduced-order modeling of advection-dominated systems with recurrent neural networks and convolutional autoencoders. *Physics of Fluids*, 33(3):037106, 2021.
- [8] Kai Fukami, Kazuto Hasegawa, Taichi Nakamura, Masaki Morimoto, and Koji Fukagata. Model order reduction with neural networks: Application to laminar and turbulent flows. *SN Computer Science*, 2(6):1–16, 2021.
- [9] Tobias Pfaff, Meire Fortunato, Alvaro Sanchez-Gonzalez, and Peter Battaglia. Learning mesh-based simulation with graph networks. In *International Conference on Learning Representations*, 2020.
- [10] Xu Han, Han Gao, Tobias Pfaff, Jian-Xun Wang, and Liping Liu. Predicting physics in mesh-reduced space with temporal attention. In *International Conference on Learning Representations*, 2022.
- [11] Nathan Baker, Frank Alexander, Timo Bremer, Aric Hagberg, Yannis Kevrekidis, Habib Najm, Manish Parashar, Abani Patra, James Sethian, Stefan Wild, et al. Workshop report on basic research needs for scientific machine learning: Core technologies for artificial intelligence. Technical report, USDOE Office of Science (SC), Washington, DC (United States), 2019.
- [12] Maziar Raissi, Paris Perdikaris, and George E Karniadakis. Physics-informed neural networks: A deep learning framework for solving forward and inverse problems involving nonlinear partial differential equations. *Journal of Computational physics*, 378:686–707, 2019.
- [13] Luning Sun, Han Gao, Shaowu Pan, and Jian-Xun Wang. Surrogate modeling for fluid flows based on physics-constrained deep learning without simulation data. *Computer Methods in Applied Mechanics and Engineering*, 361:112732, 2020.
- [14] Ruiyang Zhang, Yang Liu, and Hao Sun. Physics-informed multi-lstm networks for meta-modeling of nonlinear structures. *Computer Methods in Applied Mechanics and Engineering*, 369:113226, 2020.

- [15] Ehsan Haghighat, Maziar Raissi, Adrian Moure, Hector Gomez, and Ruben Juanes. A physics-informed deep learning framework for inversion and surrogate modeling in solid mechanics. *Computer Methods in Applied Mechanics and Engineering*, 379:113741, 2021.
- [16] Luning Sun and Jian-Xun Wang. Physics-constrained bayesian neural network for fluid flow reconstruction with sparse and noisy data. *Theoretical and Applied Mechanics Letters*, 10(3):161–169, 2020.
- [17] Amirhossein Arzani, Jian-Xun Wang, and Roshan M. D’Souza. Uncovering near-wall blood flow from sparse data with physics-informed neural networks. *Physics of Fluids*, 33(7):071905, 2021.
- [18] Lu Lu, Raphael Pestourie, Wenjie Yao, Zhicheng Wang, Francesc Verdugo, and Steven G Johnson. Physics-informed neural networks with hard constraints for inverse design. *SIAM Journal on Scientific Computing*, 43(6):B1105–B1132, 2021.
- [19] Enrui Zhang, Ming Dao, George Em Karniadakis, and Subra Suresh. Analyses of internal structures and defects in materials using physics-informed neural networks. *Science advances*, 8(7):eabk0644, 2022.
- [20] Jiequn Han, Arnulf Jentzen, and E Weinan. Solving high-dimensional partial differential equations using deep learning. *Proceedings of the National Academy of Sciences*, 115(34):8505–8510, 2018.
- [21] Dongkun Zhang, Lu Lu, Ling Guo, and George Em Karniadakis. Quantifying total uncertainty in physics-informed neural networks for solving forward and inverse stochastic problems. *Journal of Computational Physics*, 397:108850, 2019.
- [22] Yibo Yang and Paris Perdikaris. Adversarial uncertainty quantification in physics-informed neural networks. *Journal of Computational Physics*, 394:136–152, 2019.
- [23] Ehsan Kharazmi, Zhongqiang Zhang, and George Em Karniadakis. hp-vpinns: Variational physics-informed neural networks with domain decomposition. *Computer Methods in Applied Mechanics and Engineering*, 374:113547, 2021.
- [24] Ameya D Jagtap, Ehsan Kharazmi, and George Em Karniadakis. Conservative physics-informed neural networks on discrete domains for conservation laws: Applications to forward and inverse problems. *Computer Methods in Applied Mechanics and Engineering*, 365:113028, 2020.
- [25] Lu Lu, Pengzhan Jin, Guofei Pang, Zhongqiang Zhang, and George Em Karniadakis. Learning nonlinear operators via deepnet based on the universal approximation theorem of operators. *Nature Machine Intelligence*, 3(3):218–229, 2021.
- [26] Zongyi Li, Nikola Borislavov Kovachki, Kamyar Azizzadenesheli, Kaushik Bhattacharya, Andrew Stuart, Anima Anandkumar, et al. Fourier neural operator for parametric partial differential equations. In *International Conference on Learning Representations*, 2020.
- [27] Sifan Wang, Hanwen Wang, and Paris Perdikaris. Learning the solution operator of parametric partial differential equations with physics-informed deepnets. *Science advances*, 7(40):eabi8605, 2021.

- [28] Somdatta Goswami, Minglang Yin, Yue Yu, and George Em Karniadakis. A physics-informed variational deeponet for predicting crack path in quasi-brittle materials. *Computer Methods in Applied Mechanics and Engineering*, 391:114587, 2022.
- [29] Ameya D Jagtap, Kenji Kawaguchi, and George Em Karniadakis. Adaptive activation functions accelerate convergence in deep and physics-informed neural networks. *Journal of Computational Physics*, 404:109136, 2020.
- [30] Sifan Wang, Xinling Yu, and Paris Perdikaris. When and why pinns fail to train: A neural tangent kernel perspective. *Journal of Computational Physics*, 449:110768, 2022.
- [31] Sifan Wang, Shyam Sankaran, and Paris Perdikaris. Respecting causality is all you need for training physics-informed neural networks. *arXiv preprint [arXiv:2203.07404](https://arxiv.org/abs/2203.07404)*, 2022.
- [32] Han Gao, Luning Sun, and Jian-Xun Wang. PhyGeoNet: physics-informed geometry-adaptive convolutional neural networks for solving parameterized steady-state PDEs on irregular domain. *Journal of Computational Physics*, 428:110079, 2021.
- [33] Pu Ren, Chengping Rao, Yang Liu, Jian-Xun Wang, and Hao Sun. Phycrnet: Physics-informed convolutional-recurrent network for solving spatiotemporal pdes. *Computer Methods in Applied Mechanics and Engineering*, 389:114399, 2022.
- [34] Nicholas Geneva and Nicholas Zabaras. Modeling the dynamics of pde systems with physics-constrained deep auto-regressive networks. *Journal of Computational Physics*, 403:109056, 2020.
- [35] Han Gao, Luning Sun, and Jian-Xun Wang. Super-resolution and denoising of fluid flow using physics-informed convolutional neural networks without high-resolution labels. *Physics of Fluids*, 33(7):073603, 2021.
- [36] Nils Wandel, Michael Weinmann, and Reinhard Klein. Teaching the incompressible navier–stokes equations to fast neural surrogate models in three dimensions. *Physics of Fluids*, 33(4):047117, 2021.
- [37] Rishikesh Ranade, Chris Hill, and Jay Pathak. Discretizationnet: A machine-learning based solver for navier–stokes equations using finite volume discretization. *Computer Methods in Applied Mechanics and Engineering*, 378:113722, 2021.
- [38] Houpu Yao, Yi Gao, and Yongming Liu. Fea-net: A physics-guided data-driven model for efficient mechanical response prediction. *Computer Methods in Applied Mechanics and Engineering*, 363:112892, 2020.
- [39] Sebastian K Mitusch, Simon W Funke, and Miroslav Kuchta. Hybrid fem-nn models: Combining artificial neural networks with the finite element method. *Journal of Computational Physics*, 446:110651, 2021.
- [40] Zhenlin Wang, Xun Huan, and Krishna Garikipati. Variational system identification of the partial differential equations governing microstructure evolution in materials: Inference over sparse and spatially unrelated data. *Computer Methods in Applied Mechanics and Engineering*, 377:113706, 2021.

- [41] Minglang Yin, Enrui Zhang, Yue Yu, and George Em Karniadakis. Interfacing finite elements with deep neural operators for fast multiscale modeling of mechanics problems. *Computer Methods in Applied Mechanics and Engineering*, page 115027, 2022.
- [42] Han Gao, Matthew J Zahr, and Jian-Xun Wang. Physics-informed graph neural galerkin networks: A unified framework for solving pde-governed forward and inverse problems. *Computer Methods in Applied Mechanics and Engineering*, 390:114502, 2022.
- [43] Xin-Yang Liu and Jian-Xun Wang. Physics-informed dyna-style model-based deep reinforcement learning for dynamic control. *Proceedings of the Royal Society A: Mathematical, Physical and Engineering Sciences*, 477(2255):20210618, 2021.
- [44] Eldad Haber and Lars Ruthotto. Stable architectures for deep neural networks. *Inverse problems*, 34(1):014004, 2017.
- [45] Yiping Lu, Aoxiao Zhong, Quanzheng Li, and Bin Dong. Beyond finite layer neural networks: Bridging deep architectures and numerical differential equations. In *International Conference on Machine Learning*, pages 3276–3285. PMLR, 2018.
- [46] François Rousseau, Lucas Drumetz, and Ronan Fablet. Residual networks as flows of diffeomorphisms. *Journal of Mathematical Imaging and Vision*, 62(3):365–375, 2020.
- [47] Lars Ruthotto and Eldad Haber. Deep neural networks motivated by partial differential equations. *Journal of Mathematical Imaging and Vision*, 62(3):352–364, 2020.
- [48] Ben Chamberlain, James Rowbottom, Maria I Gorinova, Michael Bronstein, Stefan Webb, and Emanuele Rossi. Grand: Graph neural diffusion. In *International Conference on Machine Learning*, pages 1407–1418. PMLR, 2021.
- [49] Moshe Eliasof, Eldad Haber, and Eran Treister. PDE-GCN: Novel architectures for graph neural networks motivated by partial differential equations. *Advances in Neural Information Processing Systems*, 34, 2021.
- [50] Ricky TQ Chen, Yulia Rubanova, Jesse Bettencourt, and David K Duvenaud. Neural ordinary differential equations. *Advances in neural information processing systems*, 31, 2018.
- [51] Kaiming He, Xiangyu Zhang, Shaoqing Ren, and Jian Sun. Deep residual learning for image recognition. In *Proceedings of the IEEE conference on computer vision and pattern recognition*, pages 770–778, 2016.
- [52] Amir Gholami, Kurt Keutzer, and George Biros. Anode: Unconditionally accurate memory-efficient gradients for neural odes. *arXiv preprint [arXiv:1902.10298](https://arxiv.org/abs/1902.10298)*, 2019.
- [53] Mike Innes, Alan Edelman, Keno Fischer, Chris Rackauckas, Elliot Saba, Viral B Shah, and Will Tebbutt. A differentiable programming system to bridge machine learning and scientific computing. *arXiv preprint [arXiv:1907.07587](https://arxiv.org/abs/1907.07587)*, 2019.
- [54] Christopher Rackauckas, Yingbo Ma, Julius Martensen, Collin Warner, Kirill Zubov, Rohit Supekar, Dominic Skinner, Ali Ramadhan, and Alan Edelman. Universal differential equations for scientific machine learning. *arXiv preprint [arXiv:2001.04385](https://arxiv.org/abs/2001.04385)*, 2020.
- [55] Yifan Sun, Linan Zhang, and Hayden Schaeffer. Neupde: Neural network based ordinary and partial differential equations for modeling time-dependent data. In *Mathematical and Scientific Machine Learning*, pages 352–372. PMLR, 2020.

- [56] Andreas Hochlehnert, Alexander Terenin, Steindór Sæmundsson, and Marc Deisenroth. Learning contact dynamics using physically structured neural networks. In *International Conference on Artificial Intelligence and Statistics*, pages 2152–2160. PMLR, 2021.
- [57] Eric Heiden, David Millard, Erwin Coumans, Yizhou Sheng, and Gaurav S Sukhatme. Neural-sim: Augmenting differentiable simulators with neural networks. In *2021 IEEE International Conference on Robotics and Automation (ICRA)*, pages 9474–9481. IEEE, 2021.
- [58] Maren Hackenberg, Marlon Grodd, Clemens Kreutz, Martina Fischer, Janina Esins, Linus Grabenhenrich, Christian Karagiannidis, and Harald Binder. Using differentiable programming for flexible statistical modeling. *The American Statistician*, pages 1–10, 2021.
- [59] Dmitrii Kochkov, Jamie A Smith, Ayya Alieva, Qing Wang, Michael P Brenner, and Stephan Hoyer. Machine learning–accelerated computational fluid dynamics. *Proceedings of the National Academy of Sciences*, 118(21), 2021.
- [60] Filipe De Avila Belbute-Peres, Thomas Economou, and Zico Kolter. Combining differentiable pde solvers and graph neural networks for fluid flow prediction. In *International Conference on Machine Learning*, pages 2402–2411. PMLR, 2020.
- [61] Kiwon Um, Robert Brand, Yun Raymond Fei, Philipp Holl, and Nils Thuerey. Solver-in-the-loop: Learning from differentiable physics to interact with iterative pde-solvers. *Advances in Neural Information Processing Systems*, 33:6111–6122, 2020.
- [62] Lu Lu, Xuhui Meng, Shengze Cai, Zhiping Mao, Somdatta Goswami, Zhongqiang Zhang, and George Em Karniadakis. A comprehensive and fair comparison of two neural operators (with practical extensions) based on FAIR data. *Computer Methods in Applied Mechanics and Engineering*, 393:114778, 2022.
- [63] Bin Dong, Qingtang Jiang, and Zuowei Shen. Image restoration: Wavelet frame shrinkage, nonlinear evolution pdes, and beyond. *Multiscale Modeling & Simulation*, 15(1):606–660, 2017.
- [64] Zichao Long, Yiping Lu, Xianzhong Ma, and Bin Dong. Pde-net: Learning pdes from data. In *International Conference on Machine Learning*, pages 3208–3216. PMLR, 2018.
- [65] Zichao Long, Yiping Lu, and Bin Dong. Pde-net 2.0: Learning pdes from data with a numeric-symbolic hybrid deep network. *Journal of Computational Physics*, 399:108925, 2019.
- [66] Alvaro Sanchez-Gonzalez, Jonathan Godwin, Tobias Pfaff, Rex Ying, Jure Leskovec, and Peter Battaglia. Learning to simulate complex physics with graph networks. In *International Conference on Machine Learning*, pages 8459–8468. PMLR, 2020.
- [67] Adam Paszke, Sam Gross, Francisco Massa, Adam Lerer, James Bradbury, Gregory Chanan, Trevor Killeen, Zeming Lin, Natalia Gimelshein, Luca Antiga, Alban Desmaison, Andreas Kopf, Edward Yang, Zachary DeVito, Martin Raison, Alykhan Tejani, Sasank Chilamkurthy, Benoit Steiner, Lu Fang, Junjie Bai, and Soumith Chintala. Pytorch: An imperative style, high-performance deep learning library. In H. Wallach, H. Larochelle, A. Beygelzimer, F. d'Alché-Buc, E. Fox, and R. Garnett, editors, *Advances in Neural Information Processing Systems 32*, pages 8024–8035. Curran Associates, Inc., 2019.
- [68] Sifan Wang, Hanwen Wang, and Paris Perdikaris. Improved architectures and training algorithms for deep operator networks. *Journal of Scientific Computing*, 92(2):1–42, 2022.

[69] Dan Hendrycks and Kevin Gimpel. Gaussian error linear units (gelus). *arXiv preprint arXiv:1606.08415*, 2016.

**Acknowledgement:** X.Y.L. and J.X.W. would like to acknowledge the funds from National Science Foundation, United States of America under award numbers CMMI-1934300 and OAC-2047127. L.L. was supported by the funds from U.S. Department of Energy under award number No. DE-SC0022953.

**Author contributions:** X.Y.L., H.S. and J.X.W. contributed to the ideation and design of the research; X.Y.L. and J.X.W. performed the research (implemented the model, conducted numerical experiments, analyzed the data, contributed materials/analysis tools); M.Z. and L.L. contributed to the comparison study with other models; X.Y.L. and J.X.W. wrote the manuscript; H.S. and L.L. contributed to manuscript editing.

**Corresponding author:** Jian-Xun Wang ([jwang33@nd.edu](mailto:jwang33@nd.edu)).

**Competing interests:** The authors declare no competing interests.

**Supplementary information:** The supplementary information is attached.

# Supplementary Information for: Predicting parametric spatiotemporal dynamics by multi-resolution PDE structure-preserved deep learning

This supplementary document provides a detailed description of the proposed algorithm, examples, and numerical case settings.

## 1 Details of the neural networks

In this section, we provide the details of the implementations of the baseline methods that are omitted in the main text.

To make a fair comparison, the neural networks we used share a very similar encoder structure, which leverages multiple convolution layers (except FNO which uses channel-wise MLP) to compress the multi-channel input field to a smaller field (for PPNN, black-box ConvResNet and FNO) or to a hidden vector (for PINN and DeepONet). The physical parameters are first mapped to a field with the same shape as the input field and then passed to the CNN encoder as an additional channel. Here we use two trainable vectors (except DeepONet) of shape  $[n_x, 1]$  and  $[1, n_y]$  (where  $n_x, n_y$  are the number of evaluating points in the input field in  $x$  and  $y$  directions respectively) to generate a matrix and multiply with the physical parameters to mapping to a field.

### 1.1 PPNN and Black-box ConvResNet

The black-box ConvResNet baseline and the trainable portion of PPNN share an almost identical structure for every case, as shown in the **Extended Data Figure 1 a** and **b**, respectively. In the RD equations cases and Burgers’ equations cases, the encoder part consists of two layers of convolutional layers, using a  $6 \times 6$  kernel, with zero padding of 2 and a stride of 2. Afterwards, there are three ConvResNet blocks, each with a  $5 \times 5$  kernel, 48 channels and a zero padding of 2. In NS cases, four ConvResNet blocks are used, each of which has a  $7 \times 7$  kernel, 96 channels and a zero padding of 3. The following decoder includes a pixelshuffle with upscale factor equals 4 and a convolution layer with a  $5 \times 5$  kernel and zero padding of 2. The number of trainable parameters are shown in Tab. S1. All the neural networks are implemented on the deep learning platform PyTorch [67] and trained on a NVIDIA RTX A6000 GPU.

**Table S1:** Number of trainable parameters

| Cases      | Number of trainable parameters |                      |
|------------|--------------------------------|----------------------|
|            | PPNN                           | Black-box ConvResNet |
| RD/Burgers | 1,549,156                      | 1,548,292            |
| NS         | 5,624,869                      | 5,622,277            |

### 1.2 PINN

**Modified MLP** For PINN, we apply the modified, multi-layer perceptron (MLP) which has been “proved to be empirically & uniformly better than the conventional DeepONet architecture” [68]. The structure of this modified MLP is shown in Fig. S1(a)

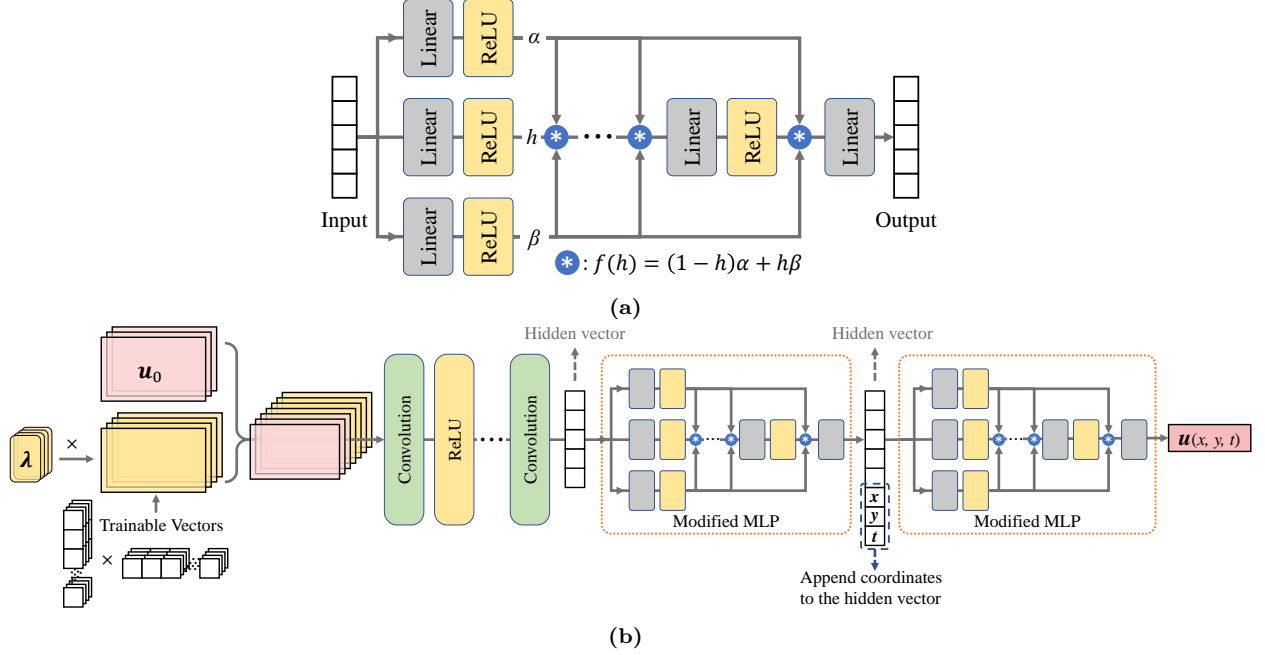


**Figure S1:** (a)Structure of modified MLP. (b) The PINN structure we used

PINN consists of a CNN encoder followed by a modified MLP to compress the input parameters: initial condition and viscosity to a hidden vector. Then the space and time coordinates are appended to the hidden vector and passed to another modified MLP. The structure is shown in Fig. S1(b). The encoder consists of 4 layers CNN, with kernel size equals to 8, 6, 6, and 8 respectively. The first three convolution layers has a stride equals to 3, while in the last layer stride equals 1. After the CNN, the field is compressed to a vector of size 48. For both modified MLPs, each has 25 hidden layers with 40000 neurons in each layer.

Because we have to evaluate the boundary values in PINN, the PINN has to deal with all the points, including those at the bottom and right boundaries which are omitted in PPNN and FNO due to these points have exact same value as those points at the top and left boundaries (periodic BC). The output is the predicted solution with two velocity components  $u_x$  and  $u_y$ . In training, the total loss  $L$  is a weighted summation of 4 components:

$$L = 20L_{IC} + L_{eq} + L_{BC} + 20L_d \quad (20)$$

initial condition loss  $L_{IC}$ , equation loss  $L_{eq}$ , boundary loss  $L_{BC}$  and data loss  $L_d$ .

### 1.3 DeepONet

We followed the description of DeepONet as proposed in [25, 62], the structure of DeepONet is shown in Fig. S2. Based on the numerical experiments, we find that use two separate neural networks to predict the two velocity components achieves slightly better performance. DeepONet consists of two parts: branch net and trunk net. The branch net is responsible for handling the hidden vector encoded from the input parameters, while the trunk net deals with the space & time coordinates. The output of these two sub-nets are element-wisely multiplied with each other and generates the output: the velocity components  $u_x$  or  $u_y$ . The DeepONet has 8 convolution layers with batch norm in the branch net, while the trunk net consists of 4 linear layers. For DeepONet-L,

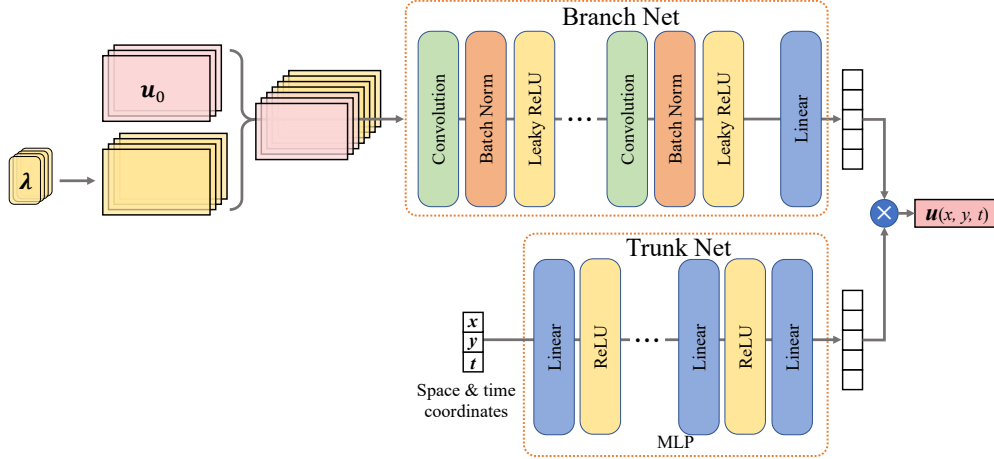


**Figure S2:** Structure of DeepONet (only shows the network used to predict  $u_x$ , the network used to predict  $u_y$  shares completely identical structure.)

the branch net contains 11 convolution layers while trunk net has 4 linear layers. For more details please refer to the source code.

## 1.4 Fourier Neural Operators (FNO)

As discussed in the main text, FNO can be formulated either as a autoregressive model like PPNN or a continuous operator like DeepONet/PINN. To distinguish the two formulations, we name the autoregressive FNO as aFNO. aFNO learns the following mapping relationship  $\mathcal{G}$ :

$$\mathcal{G} : \mathbf{u}_t; \boldsymbol{\lambda} \mapsto \mathbf{u}_{t+1}; \boldsymbol{\lambda} \quad (21)$$

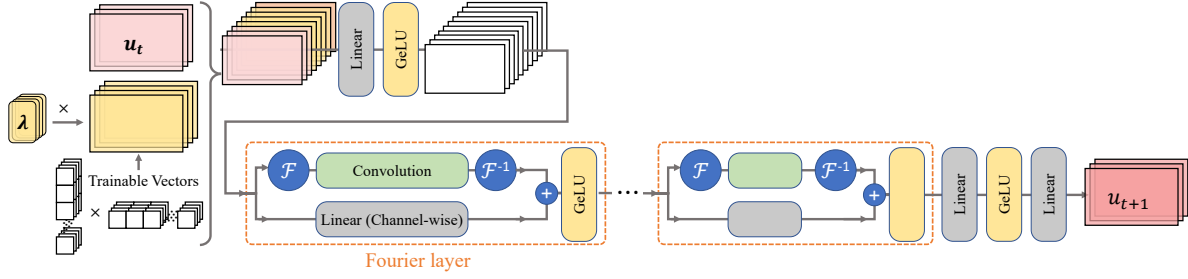
where  $\mathbf{u}$  is the state variable,  $\boldsymbol{\lambda}$  represents the physical parameters. The core component of FNO is the Fourier layer, which is shown in Fig. S3. One Fourier layer consists of two parts (as shown in the orange dash box of Fig. S3). One part contains spatial Fourier transformation, a convolution layer and inverse Fourier transformation. The other part is a channel-wise linear layer. The output of two parts are summed together. Since we want to learn a dynamic process and the evaluation position remain unchanged, we replace the original space coordinates input [26] with the time coordinate. In total there are 5 Fourier layers and each deals with 20 channels and projects to/from 12 Fourier modes. Here we follow the original FNO paper to use GeLU [69] as the activation function for every layer

The difference of the two formulations of FNOs in terms of relative error is shown in Fig. S4. Although FNO is free of the error accumulation issue, aFNO shows lower relative error in the extrapolation range. However, compared to PPNN, aFNO has a significant performance gap in both training set and testing set.

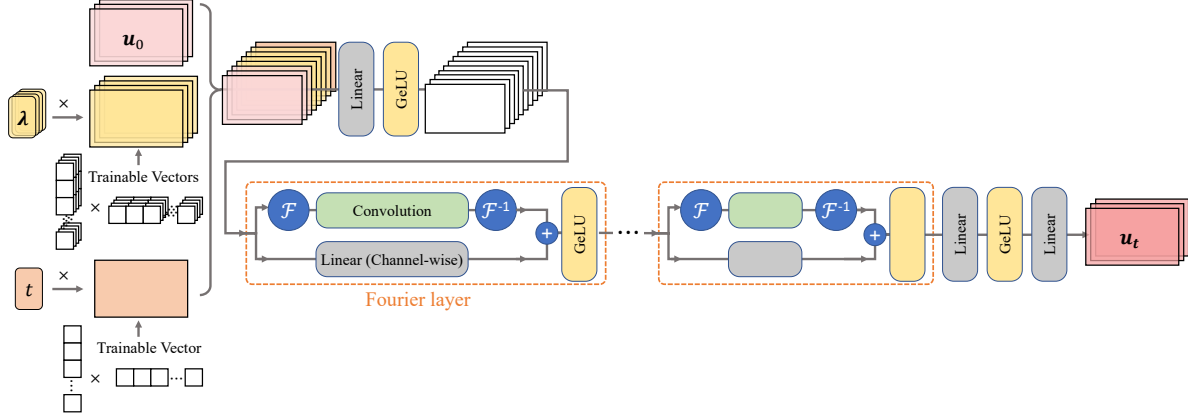
## 2 Details of the case settings and training data generation

### 2.1 FitzHugh–Nagumo reaction diffusion equations

The RD equations are solved by a finite difference solver on a  $256 \times 256$  mesh. The spatial derivatives are computed by the  $6^{th}$  order accuracy central difference scheme and time stepping is based on the forward Euler method with the time step of  $\delta t = 1 \times 10^{-5}$ . The reference solution



(a) Structure of the autoregressive FNO (aFNO)



(b) structure of continuous operator FNO (FNO)

**Figure S3:** Structure of Fourier neural operators (FNOs)

snapshots at every other 200 timesteps are collected for the neural network training, and thus the timestep size of the neural model is  $\Delta t = 200\delta t$ . The whole training dataset includes trajectories of sparse reference solutions at 8 different  $\gamma$  uniformly distributed in  $[0.6, 1.3]$  and each  $\gamma$  comes with 32 randomly generated ICs. In total, the training set contains 256 trajectories, and each trajectory includes 100 snapshots covering the temporal range of  $T = 100\Delta t$ , which starts from the 2001<sup>st</sup> numerical step. In PPNN, the PDE-preserving portion is defined on a coarse mesh of size  $48 \times 48$  with the same learning timestep size as the trainable part ( $\Delta t' = \Delta t = 200\delta t$ ).

## 2.2 Viscous Burgers equation

The Burgers' equations are solved via a finite difference solver on a  $256 \times 256$  mesh, using a  $3^{rd}$  order accuracy up-wind scheme for the convection term and  $6^{th}$  order accuracy central difference scheme for the diffusion term. Forward Euler method is used for the time stepping, with a timestep size of  $\delta t = 1 \times 10^{-4}$ . Similar to RD case, the reference solution snapshots are collected for DNN training at every other 200 numerical timesteps ( $\Delta t = 200\delta t$ ). The training dataset consists of sparse reference solutions of six different  $\nu$ , and there are 36 randomly generated ICs for each  $\nu$ . In total, the training dataset includes 216 trajectories and each trajectory includes 100 snapshots covering the temporal range of  $T = 100\Delta t$ , started from the first numerical step. In PPNN, the PDE-preserving portion is defined on a coarse mesh of size  $32 \times 32$  with the same learning step size as the trainable part ( $\Delta t' = \Delta t = 200\delta t$ ).

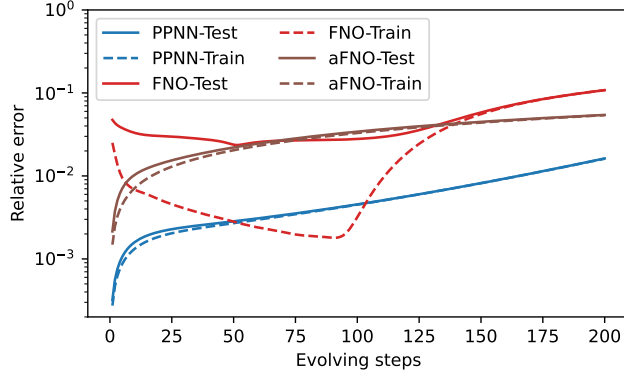


**Figure S4:** Comparison of the log-scale relative error  $\epsilon_t$  on testing parameter set (solid lines) and training parameter set (dashed lines) of the PPNN, FNO, and aFNO respectively of the velocity  $\mathbf{u}$  in the viscous Burgers' equation evaluated on 100 randomly generated testing (unseen) parameters (solid line), and 100 randomly selected training parameters. Only the first 100 time steps are used for training.

### 2.3 Naiver-Stokes equations

The N-S equation is solved on a fine mesh of  $400 \times 100$  grids using the Pressure-Implicit with Splitting of Operators (PISO) algorithm. All the numerical discretizations are conducted using OpenFOAM, which is an open-source C++ library for FVM. We simulate the NS equation for 6000 numerical steps, with numerical timestep  $\delta t = 0.01$ . The reference snapshots are collected every other 20 numerical steps, beginning from the 160<sup>th</sup> step, to form the training trajectory. Namely, the learning step is set as  $\Delta t = 80\delta t$ . In the training set, there are 45 trajectories, each of which includes 73 snapshots covering the total time of  $T = 73\Delta t$ . The same FVM discretization scheme is used to construct the PDE-preserving portion, which is defined on a coarse mesh of size  $100 \times 25$  and operated by several sub-iterations with a step size of  $\Delta t' = 2\delta t$ .

## 3 Extra contours comparison

In this section we provide contours comparison between PPNN and continuous function/operator learning methods for the viscous Burgers' case. Fig. S5 and Fig. S6 show the predicted results with training parameters at different time steps, while Fig. S7 and Fig. S8 show the predicted solution snapshots with testing (unseen) parameters. With training parameters, most methods have relatively accurate predictions within the interpolation range while once step into the extrapolation range in time ( $t \geq T$ ), PPNN shows its great generalizability over the other methods though some noise could be observed. The advantage of PPNN is even more obvious with testing (unseen) parameters. Most methods fail to give an acceptable prediction even at the first time step. While FNO gives comparable results at the first few steps, with time matching forward, PPNN show much less discrepancy from the ground truth. Besides, PPNN also keeps a very consistent performance with testing and training parameters, which indicates a great generalizability among parameters.

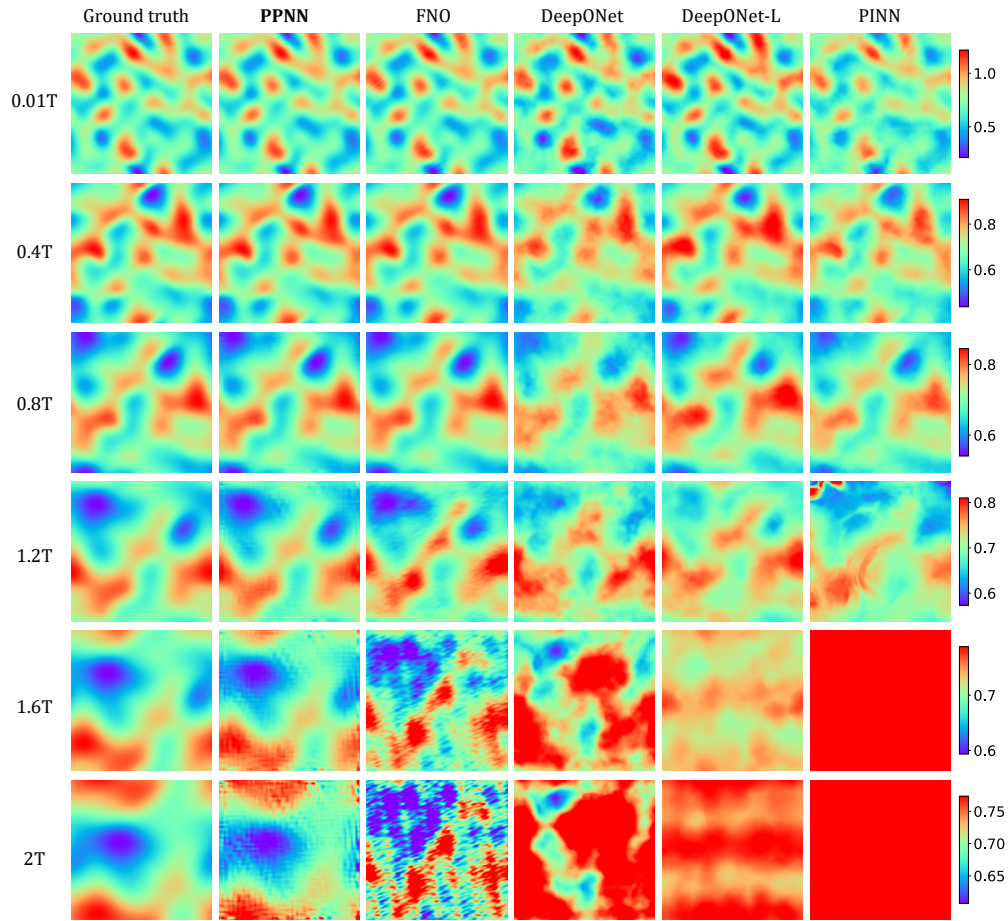


**Figure S5:** Predicted solution for the velocity magnitude  $\|\mathbf{u}\|_2$  of the Burgers' equations at different time steps and training parameters  $\lambda_9$ . Each row represents the predicted solution at a certain time step, while each column shows the results predicted by (from left to right) numerical solver (ground truth), **PPNN**, FNO, DeepONet, Pi-DeepONet, DeepONet-L, and PINN respectively.

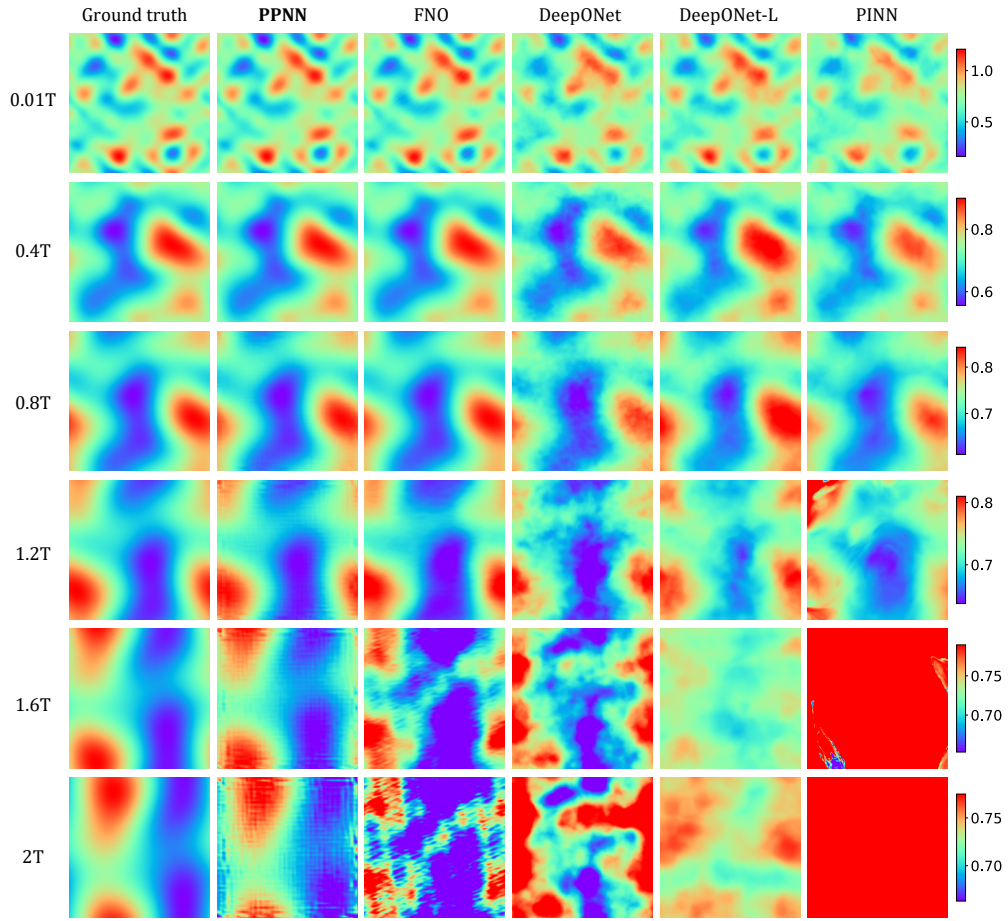


**Figure S6:** Predicted solution for the velocity magnitude  $\|\mathbf{u}\|_2$  of the Burgers' equations at different time steps and training parameters  $\lambda_{10}$ . Each row represents the predicted solution at a certain time step, while each column shows the results predicted by (from left to right) numerical solver (ground truth), **PPNN**, FNO, DeepONet, Pi-DeepONet, DeepONet-L, and PINN respectively.

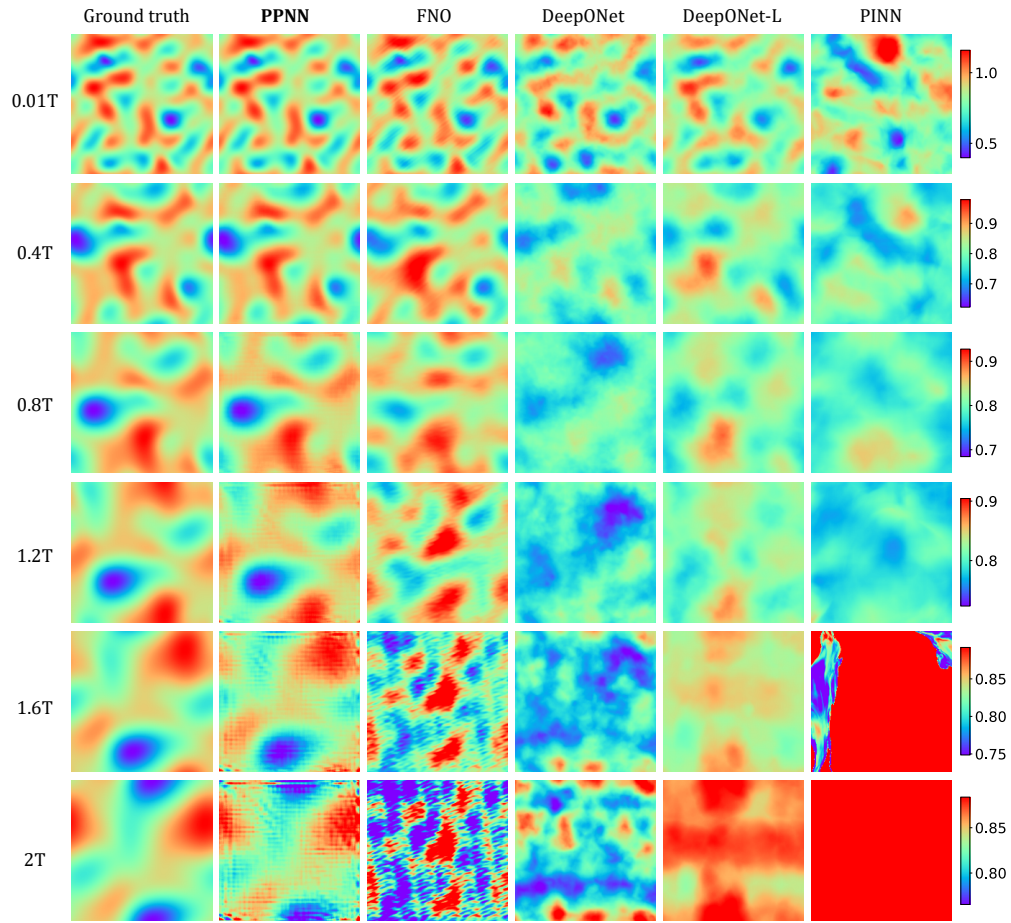


**Figure S7:** Predicted solution for the velocity magnitude  $\|\mathbf{u}\|_2$  of the Burgers' equations at different time steps and unseen parameters  $\lambda_{11}$ . Each row represents the predicted solution at a certain time step, while each column shows the results predicted by (from left to right) numerical solver (ground truth), **PPNN**, FNO, DeepONet, Pi-DeepONet, DeepONet-L, and PINN respectively.

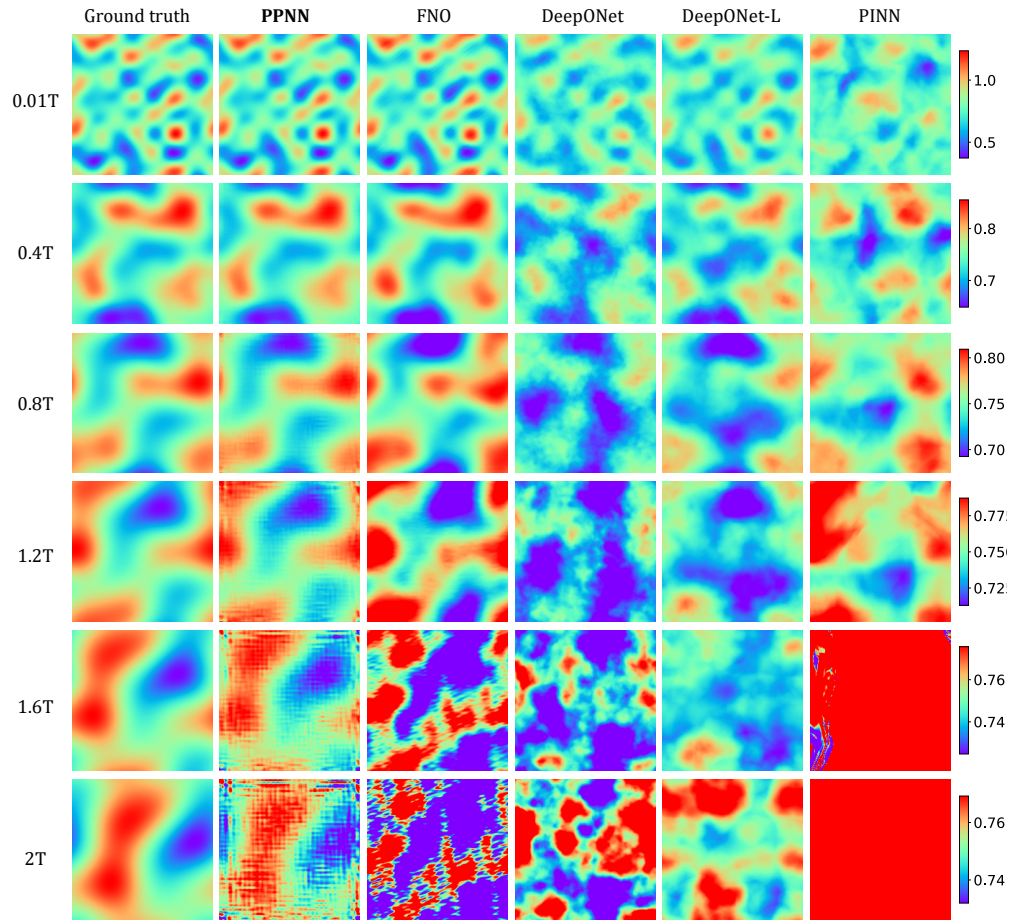


**Figure S8:** Predicted solution for the velocity magnitude  $\|\mathbf{u}\|_2$  of the Burgers' equations at different time steps and unseen parameters  $\lambda_{12}$ . Each row represents the predicted solution at a certain time step, while each column shows the results predicted by (from left to right) numerical solver (ground truth), **PPNN**, FNO, DeepONet, Pi-DeepONet, DeepONet-L, and PINN respectively.